Textural and chemical evolution of magnetite from the Paleozoic Shuanglong Fe-Cu deposit: implications for tracing ore-forming fluids

Shuanliang Zhang[1,2], Huayong Chen[1,2,3,4*], Bing Xiao[1], Liandang Zhao[5], Xia Hu[6], Jianping Li[1], Lin Gong[1,2]

1. Key Laboratory of Mineralogy and Metallogeny, Guangzhou Institute of Geochemistry, Chinese Academy of Sciences, Guangzhou 510640, China

2. University of Chinese Academy of Sciences, Beijing 100049, China

3. CAS Center for Excellence in Deep Earth Science, Guangzhou, 510640, China

4. Guangdong Provincial Key Laboratory of Mineral Physics and Materials, 511 Kehua Street, Guangzhou 510640, China

5. School of Earth Science and Resources, Chang'an University, Xi'an 710054, China

6. CAS Key Laboratory of Crust-Mantle Materials and Environments, School of Earth and Space Sciences, University of Science and Technology of China, Anhui, 230026, China

[*]Corresponding author: huayongchen@gig.ac.cn

Address: Guangzhou Institute of Geochemistry, Chinese Academy of Sciences, P.O. Box 1131, Tianhe District, Guangzhou 510640, Guangdong PRC

ABSTRACT

The Aqishan-Yamansu belt in Eastern Tianshan (NW China) hosts several important Fe and Fe-Cu deposits, the origin of which is the subject of considerable debate. The coexistence of various types of ore-forming fluids makes it difficult to distinguish the genesis of the Fe-Cu deposits. We present detailed textural and compositional data on magnetite from the Paleozoic Shuanglong Fe-Cu deposit to constrain the formation of iron oxides and the evolution of the ore-forming fluids, to define the genesis of the Fe-Cu ores.

Based on the mineral assemblages and crosscutting relationships of veins, two mineralization stages were established, including the early Fe mineralization and late Cu mineralization stage. Three types of magnetite, i.e., platy (MA), massive (MB), and granular (MC) magnetite occur in the Fe mineralization. In backscattered electron (BSE) images, an early hematite and transformational mushketovite phase (MA-I) characterized by abundant porosity and inclusions, and two later generations including an early dark (MA-II, MB-I, and MC-I) and later light magnetite (MA-III, MB-II, and MC-II) were identified, which display oscillatory zoning. The MA-I has extremely high W contents and mostly displays as micro- and invisible scheelite inclusions, which were probably caused by the W expulsion during mushketovitization. The texture and composition of magnetite suggest that the later light magnetite formed via dissolution and reprecipitation of the precursor dark magnetite, and the temperature and oxygen fugacity of fluids decreased over time.

Our study also shows the MB-II magnetite and coexisting chlorite display synchronous oscillatory zoning, with the calculated temperature from 444 to 212 ºC. Such variations could indicate the incursion of external low temperature fluids with high salinity, which can dissolve the primary dark magnetite. This study provides a good example for using magnetite to trace the complex evolution and multiple sources of ore-forming fluids.

Key words: Magnetite, Texture and chemistry, ore-forming fluid, Fe-Cu deposit, Eastern Tianshan

INTRODUCTION

Magnetite is a common mineral in many types of ore deposits, including Kiruna-type, BIF (banded iron formation), magmatic Fe-Ti oxide, Fe-skarn, IOCG and porphyry deposits, and also in many igneous, metamorphic and sedimentary rocks (Dare et al., 2014; Dupuis and Beaudoin, 2011; Hu et al., 2015; Hu et al., 2017; Huang and Beaudoin, 2019; Nadoll et al., 2014; Nadoll et al., 2012; Wu et al., 2019; Zhao et al., 2018a). It can accommodate a variety of trace elements into its inverse spinel structure by substitution with Fe^{3+} and Fe^{2+} in tetrahedral or octahedral sites (Nadoll et al., 2014), and its textures and chemical compositions vary in response to different mineralizing systems and physicochemical conditions (Dare et al., 2014; Dupuis and Beaudoin, 2011; Huang et al., 2019a; Nadoll et al., 2012). Previous studies have developed a series of discriminant diagrams to fingerprint various deposit types or ore-forming processes based on the compositional variety in magnetite (Dupuis and Beaudoin 2011; Nadoll et al., 2012). However, recently studies have also shown that the textural and chemical composition of magnetite can be significantly modified or reequilibrated by hydrothermal fluid and supergene processes (Broughm et al., 2017; Bain et al., 2020; Hu et al., 2015; Hu et al., 2014; Huang and Beaudoin, 2019; Huang et al., 2018; Wen et al., 2017; Zhang et al., 2020b), for instance, mixing with high-salinity, chlorine-rich fluids has been suggested as an important mechanism for inducing coupled dissolution-reprecipitation (DR) reactions in magnetite from hydrothermal deposits such as skarn deposits and iron oxide-copper-gold deposits (Hu

et al., 2015; Hu et al., 2014; Huang and Beaudoin, 2019; Liang et al., 2020; Yin et al., 2017).

The Aqishan-Yamansu belt in the Chinese eastern Tianshan hosts many important Fe-Cu deposits, including Heijianshan, Duotoushan, Shuanglong and Shaquanzi (Fig. 1c; Zhao et al., 2017). These Fe-Cu deposits have been described as skarns (Mao et al., 2005), but the absence of some typical features of typical skarn deposit such as the close relationships of orebodies with carbonate host rocks, and garnet-pyroxene skarn alteration, indicating that they are not typical skarn deposits. Recent studies reveal that these are possibly IOCG-like deposits according to the presence of hematite and calcite-rich Cu mineralization as well as the less amounts of pyrite, and the fluid inclusions and sulfur isotopes studies show involvement of seawater or basinal brine (Jiang et al., 2018; Zhao et al., 2017; Zhang et al., 2018b). Thus, investigation of the fluid evolution is very important for its ore genesis. As magnetite is a common mineral in these Fe-Cu deposits, the study of its texture and composition can provide important information about the ore-forming fluid and can be used to investigate the source of the mineralization. The Shuanglong system is a typical Fe-Cu deposit in the Aqishan-Yamansu belt, located in the east of the Bailingshan complex (Fig. 1c). The existence of abundant magnetite in the Shuanglong deposit provides a good opportunity to investigate the sources and evolution of ore-forming fluids during Fe and Cu mineralization based on the textural and chemical characteristics of magnetite.

We present detailed textural and compositional data, using backscattered electron

(BSE) imaging combined with electron probe microanalyzer (EPMA) and laser ablation-inductively coupled plasma-mass spectrometry (LA-ICP-MS) analyses of magnetite from the Shuanglong Fe-Cu deposit, to characterize the factors controlling the formation of the various iron oxides and the evolution of the corresponding ore-forming fluids, to constrain the genesis of the regional Fe-Cu mineralization.

GEOLOGIC SETTING

Regional geology

The Central Asian Orogenic Belt (CAOB; Fig. 1a) is a complex collage of ophiolite suites, magmatic arc remnants, accretionary wedges, and continental fragments (Sengor, 1996; Sengor et al., 1993; Windley et al., 2007), which formed during the evolution of the Paleo-Asian Ocean (PAO) through a long period from the Neoproterozoic to Neopaleozoic (Han and Zhao, 2018; Sengor et al., 1993; Windley et al., 2007; Xiao et al., 2013). The Eastern Tianshan, situated to the north of the Tarim Basin in North Xinjiang (Fig. 1b), can be divided into the Dananhu-Tousuquan Island Arc Belt, Kangguer Shear Zone, and Aqishan-Yamansu Belt (from north to south) by the E-W-trending Kangguer and Yamansu faults (Fig. 1c).

The Dananhu-Tousuquan Island Arc Belt is situated to the north of the Kangguer shear zone and contains Devonian to Carboniferous volcanic and plutonic rocks, and hosts several porphyry copper deposits, including the Tuwu-Yandong deposit (Fig. 1c; Mao et al., 2005). The Kangguer Shear Zone is an important regional structure that

separates the Junggar Block from the Tarim Block (Chen et al., 2019), and contains ductility deformed Carboniferous volcaniclastic rocks that have been metamorphosed to greenschist facies (Xiao et al., 2004) and Permian mafic-ultramafic intrusions (Qin et al., 2011). The shear zone hosts Au deposits in the west (e.g., Shiyingtan and Kangguer; Xiao et al., 2004) and Cu–Ni deposits in the east (e.g., Huangshan and Huangshandong; Fig. 1c; Qin et al., 2011).

The Aqishan-Yamansu Belt (Fig. 1c) contains mainly Carboniferous volcanic, volcaniclastic, and clastic rocks overlain by Permian clastic and volcanic rocks with local carbonate interbeds (Mao et al., 2005). The Carboniferous rocks consist of the Early Carboniferous Yamansu and Late Carboniferous Tugutubulak formations (Zhao et al., 2018b). Late Carboniferous to Early Triassic felsic intrusions intruded the Carboniferous Aqishan-Yamansu strata (Zhao et al., 2018b; Zhou et al., 2010), and are associated with Fe- and Fe-Cu deposits, including Hongyuntan, Bailingshan, Chilongfeng, Heijianshan, Yamansu, and Shaquanzi (Huang et al., 2018; Jiang et al., 2018; Zhao et al., 2017). Previous studies have proposed that the Aqishan-Yamansu belt represents an arc-related basin formed by southward subduction of the Kangguer oceanic plate beneath the Central Tianshan block during the Early Carboniferous (350–330 Ma), and the basin was then inverted during the Late Carboniferous (320–305 Ma; Zhang et al., 2020b).

Ore deposit geology

The Shuanglong Fe-Cu deposit is located ~260 km south of Hami city, NW China. The Shuanglong deposit is hosted in the Upper Carboniferous Tugutubulak Formation which can be subdivided into three members: the lower member consisting of basalt, volcanic breccia and volcanic tuff which is volcanic explosive facies, the middle member which is volcanic overflowing facies of volcanic tuff and rhyolitic ignimbrite, and the upper member which is volcano-sedimentary facies, comprising mainly andesitic tuff with carbonate interlayers. These volcanic rocks and volcaniclastic rocks all belong to the calc alkali series. Previous studies have shown that the volcanic tuff in the Shuanglong deposit has LA-ICP-MS zircon U-Pb ages of 319.1 ± 1.9 Ma to 305.4 ± 1.6 Ma (Zhang et al., 2020b). The Tugutubulak Formation at Shuanglong was intruded by the Bailingshan intrusive complex, including diorite (317.1 ± 3.3 Ma; Zhang et al., 2020), monzogranite (311.0 ± 1.4 Ma; Zhang et al., 2020b), granodiorite (307.5 ± 1.7 Ma; Zhao et al., 2019), and minor granite and granite porphyry (306.9 ± 1.7 Ma; Fig. 2; Zhang et al., 2020b). Multiple faults have been recognized in the Shuanglong ore district, and the ore bodies are associated with the E- trending Shuanglong fault (Fig. 2).

Two ore zones have been defined in the Shuanglong district. The main Fe-Cu orebody (L3) occurs in the northern zone, extending for approximately 120 m in length with a width ranging from 9 to 27m (Fig. 2). The orebody was controlled by the Shuanglong faults, and its dip direction is consistent with the fault dip and infilled

in the fault. The host rocks of the orebody are Carboniferous Tugutubulak Formation volcaniclastic rocks and diorite intrusions. The ore minerals consist primarily of magnetite, hematite, and sulfides including pyrite, pyrrhotite, and chalcopyrite. The wall rock alteration includes garnet (andradite), K-feldspar, epidote, amphibole (actinolite), quartz, calcite, and chlorite (pycnochlorite) alteration. Three hydrothermal alteration and mineralization stages can be identified at Shuanglong, namely (I) Skarn alteration, (II) Fe mineralization, and (III) Cu mineralization (Fig. 3).

Stage I skarn alteration contains abundant garnet occurring as euhedral to subhedral fine-grains in the magnetite ore and wall rock and is commonly replaced or cut by the Stage II K-feldspar-magnetite veins. The stage II Fe mineralization mainly contains platy mushketovite that coexists with amphibole (Fig. 4a–b), massive magnetite that occurs with amphibole, chlorite, quartz and pyrite (Fig. 4c–d), and disseminated magnetite with K-feldspar, or epidote-amphibole in wall rocks that has undergone early K-feldspar alteration and secondary epidote-amphibole-(-calcite) alteration (Fig. 4e–f). In addition, residual hematite can be found in the cores of the mushketovite (Fig. 4b), indicating that hematite stage occurred before the magnetite. Stage III Cu mineralization is dominated by veins or aggregates of quartz-hematite-chalcopyrite (Fig. 4g-h), and epidote-calcite-hematite -chalcopyrite, with locally minor chlorite.

SAMPLING AND ANALYTICAL METHODS

Representative samples of three types of magnetite from Stage II Fe mineralization were selected for this study. The magnetite samples include platy magnetite (MA Mag - SL16-6, SL16-8, SL17-157) and massive magnetite (MB Mag - SL17-116, SL17-118) collected from the ore bodies, as well as disseminated magnetite (MC Mag - SL17-88, SL17-136, SL17-137) from the wall rocks. The chlorite and pyrite which coexist with magnetite were also selected for analysis in this study, including chlorite in platy magnetite sample (SL17-157) and massive magnetite sample (SL17-116, SL17-118), and pyrite in platy magnetite sample (SL17-157), massive magnetite sample (SL17-116) and disseminated magnetite sample (SL17-88). All samples were prepared as standard polished thin sections and subsequently analyzed for their textural characteristics by Scanning Electron Microscope (SEM) in backscattered electron (BSE) mode, and magnetite, chlorite and pyrite major chemistry by Electron Probe Micro-Analyzer (EPMA), and magnetite trace element geochemistry by Laser Ablation Inductively Coupled Plasma Mass Spectrometry (LA-ICP-MS).

The representative sample sections were carbon coating and then investigated with a ΣIGMA SEM in BSE mode, at Guangzhou Institute of Geochemistry, Chinese Academy of Sciences (GIGCAS). The major element geochemistry of magnetite, chlorite, and pyrite was analyzed using a JEOL JXA-8230 electron microprobe at the Shandong Analysis Center of China Metallurgical Geology Bureau. The operating

conditions were 15 kV accelerating voltage, 20 nA beam current, 1 μm beam diameter, 10 s counting time and ZAF correction procedure for the data reduction. Zoning in magnetite grain was mapped using EPMA for Fe, Si, Ti, Al, Mn, and V, and zoning in chlorite grain was mapped for Si, Fe, Al and Mg. The operating conditions were 20 kV voltage, 300 nA probe current, 0.5 to 4 μm beam size, and a dwell time of 100 to 200 ms for each point were used for mapping.

Magnetite trace element geochemistry was analyzed by LA-ICP-MS at the In Situ Mineral Geochemistry Lab, Ore Deposit and Exploration Centre (ODEC), Hefei University of Technology, Hefei, Anhui Province, China. The analyses were carried out on an Agilent 7900 Quadrupole ICP-MS coupled to a Photon Machines Analyte HE 193-nm ArF Excimer Laser Ablation system. Argon was used as the make-up gas and mixed with the carrier gas via a T-connector before entering the ICP (Ning et al., 2017; Wang et al., 2017). Each analysis was performed with a uniform spot size diameter of 30mm at 8 Hz with an energy of ~4 J/cm^2 for 40s after measuring the gas blank for 20s. Standard reference materials NIST 610, NIST 612, BCR-2G, and MASS-1 were used as external standards to plot calibration curves using preferred element concentrations for the USGS reference glasses from the GeoReM database (http://georem.mpch-mainz.gwdg.de/). Off-line data processing was undertaken using the ICPMS Data Cal software package (Liu et al., 2008), and ^{57}Fe was used as internal standardization.

RESULTS

Petrography and texture of magnetite and chlorite

As mentioned above, the magnetite in the Shuanglong deposit is composed of platy (MA), massive (MB) and granular (MC) types from the Stage II Fe mineralization stage. The MA magnetite commonly coexists with amphibole and shows three different zones in BSE images (central light, median dark, and outer light; Fig. 5a-b), indicating that it may have evolved through three generations. The light magnetite (MA-I) in the core is characterized by residual hematite, abundant porosity and inclusions that commonly consist of tiny W-bearing minerals such as scheelite (Fig. 5b) and is commonly overgrown by the later dark MA-II magnetite that grows parallel to the contact interface of MA-I magnetite (Fig. 5b). Median dark magnetite (MA-II) is characterized by abundant silicate inclusions (i.e., amphibole) and weak to obvious oscillatory zoning including dark and light bands (MA-IID and MA-IIL; Fig. 5b). The outermost light magnetite (MA-III) lacks porosity and inclusions, and several dark bands occur within its rim (MA-III; Fig. 5b).

The MB magnetite occurs as aggregates of euhedral grains, coexisting with amphibole, minor chalcopyrite and chlorite (Fig. 4c-d). It shows two generations including primary dark magnetite which is characterized by well-developed oscillatory zoning, and secondary light magnetite (Fig. 5d). In the primary dark magnetite with oscillatory zoning, the dark magnetite (MB-ID) has been overgrown

by later light magnetite (MB-IL), and abundant porosity in the light magnetite (Fig. 5d). Complete MB-I magnetite grains have been replaced by secondary MB-II light magnetite, with abundant porosity and inclusions such as chlorite and chalcopyrite, distributed in the secondary MB-II magnetite at the interface between MB-I and MB-II magnetite (Fig. 5d and f). In addition, some MB-II also overgrown with primary dark magnetite grain and display oscillatory zoning with dark bands (Fig. 5d).

The MB-II magnetite mainly coexists with chlorite, as shown in the micro-inclusions and cracks (Fig. 6a). The chlorite occurs as pseudo-uniaxial plates arranged in rosette shaped aggregates (Fig. 6a and b). SEM images show that rosette chlorite displays oscillatory zoning pattern and mainly include two zones (Fig. 6a and b), the zone 1 is composed of stacks of 20-80 μm thick layers, suggesting that the primary chlorite grew in an open space. Chlorite in zone 2 overgrows along the crystal in zone 1 and some also exists as euhedral to subhedral crystals. Chlorite in both zones show alternated dark and light bands, and the zone 2 chlorite coexists with outermost layer of MB-II magnetite (Fig. 6a).

The MC magnetite commonly occurs as euhedral or subhedral granular magnetite in the wall rock, accompanied by two stages of alteration an early K-feldspar (-calcite) phase and a late epidote-amphibole phase, where the K-feldspar is replaced by later epidote and calcite (Fig. 5g). These two phases of alteration may also be reflected in the textures of the magnetite, as the primary dark magnetite (MC-I) has been replaced by the secondary light magnetite (MC-II) which coexists with

epidote (Fig. 5g-h), and the MC-I magnetite probably formed with the early K-feldspar based on the sequence of alteration identified in wall rock.

Therefore, based on the petrography and texture of the different types of magnetite, they can be divided into three phases an early MA-I mushketovite, a second phase including MA-II, MB-I, and MC-I magnetite which occur as "dark bands" in BSE images; and the third phase of magnetite including MA-III, MB-II, and MC-II which occur as "light bands" in BSE images.

EPMA

The EPMA elemental mapping shows that the three generations in MA magnetite including the first generation of MA-I magnetite transformed by precursor hematite, and the later phrases (MA-II and MA-III) are overgrown with it. And the dark magnetite (MA-II) contains higher content of Si, Al, but lower Fe content than the light magnetite (MA-I and MA-III; Fig. 7a). In the MB magnetite, the dark magnetite (MB-I) contains higher content of Si, Al, but lower Fe and V contents than light magnetite (MB-II; Fig. 7b). For the dark and light bands in the oscillatory zoned MB-I magnetite displays similar variations trend as the dark MB-ID magnetite contains higher Si, Al, and lower Fe contents than that of light MB-IL magnetite (Fig. 7b). The EPMA elemental mapping shows that the dark zone in MC magnetite (MC-I) contains higher contents of Si and Al, but lower Fe contents than the light magnetite (MC-II; Fig. 7c).

A total of 201 EPMA spot analyses were completed on the magnetite, with 30 spots on MA-I, 29 on MA-IID, 21 on MA-IIL, 36 on MA-III, 27 on MB-ID, 11 on MB-IL, 17 on MB-II, 13 on MC-I and 18 on MC-II. The full results of chemical contents of the Shuanglong magnetite are presented in in Table 1. Figure 8a shows comparative box and whisker diagrams of major elements in the various magnetite generations.

The mushketovite (MA) contains three generations of magnetite, and the MA-II magnetite with oscillatory zoning has dark and light zones (MA-IID and MA-IIL), thus corresponding to four compositional groups (Fig. 7a). MA-I magnetite has the highest average Fe (72.9 wt%), the lowest Si (0.03 wt%), Al (0.02 wt%), Ca (0.03 wt%), Mn (0.08 wt%) and Ti (0.03 wt%), and the contents of Mg, V, Cr and Ni are mostly below the detection limit; MA-IID magnetite has the lowest average Fe (68.5 wt%), the highest average Si (1.4 wt%), Al (0.43 wt%), Ca (0.68 wt%), Mg (0.08 wt%), Mn (0.13 wt%), Ti (0.03 wt%); MA-IIL magnetite contains moderate average Fe (67.0 wt%), and moderately high average Si (0.94 wt%), Al (0.22 wt%), Ca (0.42 wt%), Mg (0.06 wt%); MA-III magnetite has similar composition with MA-I, containing (average) contents of Fe (72.2 wt%), Si (0.19 wt%), Al (0.09 wt%), Ca (0.25 wt%), Mn (0.08 wt%), Ti (0.04 wt%), and Mg (0.02 wt%), and with the contents of Cr and Ni mostly below the detection limit.

The MB magnetite contains two generations, and the primary generation (MB-I) contains obvious oscillatory zoning including dark and light zones (MB-ID and

MB-IL). MB-ID magnetite has the lowest average Fe (68.8 wt%), the highest average Si (1.07 wt%), Al (0.52 wt%), Ca (0.56 wt%), Mg (0.07 wt%), and Ti (0.11 wt%); MB-IL magnetite contains moderately low average Fe (70.0 wt%), and moderately high average Si (0.73 wt%), Al (0.33 wt%), Ca (0.40 wt%), Mg (0.05 wt%), and Ti (0.06 wt%); MB-II magnetite has the highest average Fe (72.1 wt%), the lowest Si (0.11 wt%), Al (0.03 wt%), Ca (0.04 wt%), and Ti (0.05 wt%). All the MB magnetite subtypes contain similar Mn (0.072, 0.071, 0.058 wt%, respectively) and V (0.024, 0.024, 0.03 wt%, respectively). The concentrations of Ni and Cr are mostly below the detection limit. For the MC magnetite, MC-I magnetite has higher average Si (0.69 wt%), Al (0.16 wt%), Ca (0.36 wt%), Mg (0.04 wt%), Mn (0.14 wt%), Ti (0.04 wt%), V (0.06 wt%), and lower average Fe (70.0 wt%) compared to MC-II magnetite which has the lower average Si (0.18 wt%), Al (0.02 wt%), Ca (0.06 wt%), Mg (0.01 wt%), Mn (0.1 wt%), Ti (0.03 wt%), V (0.04 wt%) and higher average Fe (69.2 wt%); and the concentrations in Ni and Cr of both subtypes are mostly below the detection limit.

The tungsten inclusions in MA-I magnetite have also been analyzed by EPMA, however, due to its extremely small size, the data seems to be a mixture with magnetite. Even so, the analyses reveal high Ca (5.4-6.4 wt%) and W (19.3-28.6 wt%) contents, with significant Mo (0.6-0.9 wt%; Appendix Table 1).

The EPMA elemental mapping shows that the alternated dark and light bands in chlorite have compositional variations, the dark bands contain higher content of Si, Mg, but lower Fe and Al content than the light bands (Fig. 6). The EPMA spot

analysis shows that the oscillatory contrasts are mainly caused by FeO and MgO content variation. The average FeO and MgO content in zone 1 have variations from dark (21.7 wt%, 17.8 wt%; Appendix Table 1) to light bands (25.9 wt%, 14.7 wt%), and ranges from dark (19.5 wt%, 18.8 wt%) to light bands (24.8 wt%, 15.9 wt%) in zone 2. SiO_2 and Al_2O_3 contents show smaller variations (less than 2 wt%). The EPMA spot analysis shows that the pyrite which coexists with magnetite has variable and high Co and Ni contents (0.19-1.54 wt%, 0.02-0.25 wt%).

LA-ICP-MS

Due to the small-scale oscillatory zoning in MA-II and MB-I magnetite, light and dark domains of magnetite could not be separately measured by LA-ICP-MS, and thus, analytical results of MA-II and MB-I magnetite represent the average composition of light and dark domains in oscillatory zoning. Full LA-ICP-MS analytical results and the corresponding detection limits are provided in Appendix Table 1 and illustrated in Figure 8b. Most of the data for Cu and rare earth elements (REE) are below detection limits. In general, the dark magnetite including MA-II, MB-I, and MC-I magnetite have higher Mg, Al, Si, Ca, Ti, Zn, Ga, and Sr concentrations than those in the light magnetite including MA-III, MB-II, and MC-I. The mushketovite including MA-I and MA-II magnetite have relatively high W (69-3311 ppm; 1-271 ppm), Sn (1.2-31.7 ppm; 1.1-14.6 ppm), and U (2.7-78.6 ppm; 0.2-1.9 ppm) concentrations than other magnetite subtypes, although the content of

these elements in other magnetite types is all below 1 ppm or below the detection limit (Appendix Table 1).

The statistical techniques (factor analysis) were used in this study, to examine underlying relations among elements content obtained with LA-ICP-MS. We used a principal component extraction method with a Kaiser Varimax rotation (Kaiser, 1958) and a Bartlett factor score (Bartlett, 1937). Factors score coefficients for each analysis are derived from the factor loadings. The factor score represents the significance of a given factor for an analysis. The factor score line outside -0.5 to 0.5 indicate significant relations. The factor analysis results provide three multiple elements factors: factors 1 comprising Si, Al, Ca, Mg, Sr, Mn and Co, factors 2 comprising Ti, Ga and Zn, and factors 3 comprising V, Ni, Cr and Sc (Fig. 9).

DISCUSSION

Controlling factors for magnetite composition

Magnetite has a general stoichiometry XY_2O_4, where X is divalent cations such as Mg, Fe, Mn and Ni, and Y represents trivalent or tetravalent cations such as Si, Al, Fe and V. For the EPMA results, positive correlations ($R^2 \geq 0.7$) are exhibited among Si, Al, Ca, Mg and Mn, and Ti positively correlates with Al ($R^2=0.6$), whereas Ti and V do not correlate with any of the other trace elements. The factor analysis of LA-ICP-MS results also reveal three factors (Fig. 9), suggesting that some trace elements have underlying correlation, e.g., Si, Ca, Al, Mg, Mn, Sr, Sn and Co; Ti, Zn

353 and Ga; V, Ni, Sc and Cr. These correlations of trace elements could probably be
354 attributed to several reasons, such as the inclusions (amphibole) and partition
355 coefficient. Fe^{3+} is negatively correlated with Si and Al (Fig. 10a), indicating that
356 these elements were incorporated into the structural sites of magnetite by substitution
357 of Si^{4+} and Al^{3+} for Fe^{3+}. Si also positively correlates with Ca and Mg, indicating
358 these divalent elements play as a valence state balance related to the substitution. Fe^{2+}
359 is negatively correlated with Ca and Mg (Fig. 10b), indicating Mg^{2+} and Ca^{2+}
360 substitute Fe^{2+}. Micro-inclusions or nano-inclusions in magnetite can influence the
361 magnetite geochemistry detected. For MA-I magnetite, the few anomalously high W
362 and Ca signal may point to the presence of invisible W-bearing micro-inclusions (Fig.
363 11a and b), probably be scheelite ($CaWO_4$), and few visible scheelite inclusions were
364 also found in MA-I magnetite (Fig. 5b). Moreover, the positive correlate between W
365 and Mn indicate the invisible wolframite ((Fe, Mn) WO_4) inclusions may occur (Fig.
366 12h). However, some spots show extremely high W content with stable signal,
367 indicating W may also incorporate into the lattice of magnetite (Fig. 11c). For other
368 magnetite, especially the trace element rich zone, our EPMA spot analyses can avoid
369 the visible inclusions, however, most LA-ICP-MS analyses could not avoid
370 nano-scale inclusions. For example, the positive correlate between Sr and Al, Ca may
371 be caused by the silicate inclusions due to that Sr is highly incompatible for magnetite
372 (Fig. 12f and g, Nielsen et al., 1994).

373 The composition of magnetite is mainly controlled by some factors including: (1)

co-precipitating minerals (mainly Fe-sulfides), (2) fluid geochemistry and rock-water reaction, and (3) physicochemical conditions including temperature and oxygen fugacity (Whalen and Chappel, 1988; Frost and Lindsley, 1991; Ghiorso and Sack, 1991). The presence of other minerals within the mineral assemblage has significant effect on magnetite geochemistry. Minerals coprecipitated with magnetite can preferentially partition some certain elements, for instance, chalcophile (e.g., Cu, Co, Pb) and siderophile elements (e.g., Ni) preferentially partition into sulfides minerals (Cygan and Candela 1995; Fleet et al., 1996; Simon et al. 2008), whereas lithophile elements (e.g., Mg, Al, Si, Ti) partition into silicates minerals (Frost 1991; Toplis and Corgne 2002). The MA and MB magnetite produced from infilling coexist with similar minerals, primary dark magnetite with mainly amphibole and secondary light with mainly chlorite and few pyrite, whereas the MC magnetite was produced by K-Fe and subsequent Ca-Fe alteration. The MB and MC have similar low Cu, Pb, Co and Ni contents (Fig. 8b), however the rare coexisting pyrite has extremely high Co and Ni contents (0.19-1.54 wt%, 0.02-0.25 wt%), indicating that coexisting sulfides effectively scavenge certain elements. Although some difference in lithophile elements (Fig. 8a, MA has higher Si, Al, Mg, Ca, Sr contents), it is difficult to know what caused it due to the influence of potential nano silicate inclusions, and such systematic difference was probably controlled by the fluid geochemistry or degree of rock-water reaction. Extensive fluid-host rock interaction commonly results in hydrothermal magnetite enriching in Si, Al, Mg and Mn (Carew 2004; Nadoll et al.

2014; Deditius et al. 2018). The MC magnetite has low Si, Al, Mg, and Mn contents (Fig. 8a), reflecting a low degree of fluid-rock interaction, and the MC has high Mn content probably due to the recharge of Mn during K-Fe alteration (Corriveau et al. 2016). In addition, MA magnetite samples have significant W, Sn, Pb, and U contents which are basically below the detection line in MB and MC (Fig. 8b), and these elements are actually concentrated in MA-I (core of MA). Considering that MA-I was transformed from hematite, it may represent the compositional information of the original hematite.

Little experimental result is currently available on the partitioning efficiency of trace elements between magnetite and hydrothermal fluids (Chou and Eugster, 1977; Ilton and Eugster, 1989; Simon et al., 2004). It is generally considered that some factors such as temperature and oxygen fugacity control partitioning of trace elements in hydrothermal-derived magnetite like that in igneous system. For example, Al and Ti concentrations in igneous-derived magnetite are high positively correlative with temperature (Nielsen et al.,1994; Toplis and Carroll, 1995), and these elements also decrease from high-temperature porphyry and skarn magnetite to low-temperature banded iron formation (BIF) (Nadoll et al., 2014). For the oscillatory zoning in MA-II and MB-I magnetite (Fig. 8a), it is clear that the light bands (MB-IL) have lower Ti contents than the dark bands (MB-ID, D and L mean dark and light bands), however, no obvious differences in Ti content were observed between dark (MA-IID) and light (MA-IIL) bands in MA-II magnetite (Fig. 8a), likely due to the very low abundances.

Combined with the decrease of trace element such as Al and Mg being related to temperature in MA-II and MB-I magnetite, it is likely that the oscillatory zoning in MA-II and MB-I magnetite was mainly controlled by changes in temperature. The above factor analysis result also shows that Ti, Ga and Zn have correlations (Fig. 9, 12a and 12b). Nadoll et al. (2014) proposed that Ga concentration follows the trend that highest concentrations are in high temperature igneous magnetite and the lowest in BIF magnetite. Previous study also showed that Zn is more effectively fractionated into hydrothermal fluids than Fe with decreasing temperature (Ilton and Eugster 1989; Wu et al., 2019). Therefore, Ga and Zn in Shuanglong magnetite were also controlled by temperature. Nadoll et al. (2014) proposed the Ti + V vs. Al + Mn plot can reflect the variation in temperature, with high-temperature magnetite plotting at high values of Ti + V and Al + Mn values. The Shuanglong magnetite displays a descending temperature trend suggesting they formed from a fluid under middle to high-temperature conditions > 200 ℃ (Fig. 13; Deditius et al., 2018; Nadoll et al., 2014). Some elements, such as V and Cr, can occur in various valence states (e.g., V^{3+}, V^{4+}, V^{5+}), and therefore, their behavior is strongly linked to fO_2 (Nadoll et al., 2014; Toplis and Carroll, 1995; Toplis and Corgne, 2002). For example, Toplis and Corgne (2002) proposed vanadium partitioning is strongly dependent on oxygen fugacity, decreasing by approximately one order of magnitude with increasing fO_2 from NNO-0.7 to NNO+2.6 for magnetite at a constant temperature (1068 ℃), and this behaviour is inferred to be dominated by partitioning of V^{3+} due to the relative

proportions of V^{n+} (Toplis and Corgne, 2002). However, it is less well constrained at cooler temperature hydrothermal fluids (Nadoll et al., 2014). The MA magnetite has low V contents, reflecting a more oxidized fluid. For the dark zone and light zone in MA and MB magnetite, the contents of V were slightly increased, indicating the decreasing of oxygen fugacity in fluids which is consistent with the coexisting pyrite in light magnetite. The Ni content also shows strong positive correlation with V (Fig. 12c), probably also related with the oxygen fugacity. Moreover, the EPMA data show that the V content of MC-II decreases obviously compared to MC-I (Fig. 8a), revealing an opposite trend.

Tungsten remobilization during mushketovitization

Previous studies have shown that platy magnetite (also call mushketovite) is common in IOCG deposits, such as the Heijianshan deposit in Eastern Tianshan and the Candelaria deposit in Chile (Marschik, 2001; Zhao et al., 2018a). The mushketovite is interpreted to result from transformation of magnetite after hematite during reducing fluid reactions, a process called mushketovitization (Hu et al., 2020; Mucke and Cabral 2005; Ohmoto, 2003). At Shuanglong, abundant platy magnetite (MA Mag) coexists with actinolite, pyrite and chlorite. In fact, only the core of MA magnetite is the result during the reducing reactions according to the presence of residual hematite and abundant micro porosity probably formed by the volume shrinkage during the reactions (Hu et al., 2020; Mucke and Cabral 2005).

457 Significantly, abundant scheelite inclusions occur in the MA-I magnetite, and the
458 previous discussion revealed that the high W contents of MA-I were also attributed to
459 invisible scheelite inclusions and lattice-tungsten. Measured partition coefficients for
460 igneous magnetite indicate that W is highly incompatible (Klemme et al., 2006),
461 however, some authors have reported the incorporation of W into magnetite at
462 significant levels (up to dozens of ppm; Candela, 1997; Carew, 2004; Huang et al.,
463 2019). Thus, such a high contents in mushketovite could have been inherited from the
464 precursor hematite. Indeed, W-U-Sn-Mo enriched hematite is common in many
465 hydrothermal deposits, such as the Olympic Dam Cu-U-Au-Ag deposit (Ciobanu et
466 al., 2013; Verdugo-Ihl et al., 2017), and these element were incorporated into the
467 structural sites of magnetite by: $2Fe^{3+} \leftrightarrow Me^{6+} + \square$, in which the Me could be U, W
468 and Pb (Ciobanu et al., 2013). Verdugo-Ihl et al. (2020) also proposed significant W
469 can be released from hematite due to coupled dissolution–reprecipitation during
470 interaction with fluids, and was confirmed at nanoscale. Therefore, when
471 mushketovitization of hematite occurred, the reduction in volume results in abundant
472 porosity and cracks which provide pathways for fluid percolation and the release of W.
473 In addition, the estimate values of fO_2 for many scheelite or wolframite deposits
474 mostly lie between quartz-fayalite-magnetite (QFM) and Ni-NiO (NNO) buffers
475 (Wood, 2000 and reference therein), and no tungsten inclusions have been found in
476 the hematite, indicating that these inclusions are not coexisting with the previous
477 hematite. Therefore, these scheelite inclusions might be released from the previous

hematite and precipitated in open spaces due to local supersaturation.

Origin of synchronous oscillatory zoning in magnetite-chlorite aggregates

Oscillatory zoning in MA and MB magnetite is very common in Shuanglong deposit and can be divided into two phases in MA-II, MB-I, and MA-III, MB-II respectively. They are composed of alternately dark and light bands under BSE imaging. The coexisting mineral chlorite occurring as rosette-shape can be divided into two oscillatory zones. Similar oscillatory zoning in magnetite is widely observed in Fe skarn deposit (Dare et al., 2014; Huang et al., 2018), IOCG deposit (Huang et al., 2019) and IOA deposit (Knipping et al., 2015b; Deditius et al., 2018). A common explanation for the oscillatory zoning in magnetite is that the changes in fluid compositions and/or physicochemical parameters (such as temperature and oxygen fugacity) during the crystal growth, that could also periodically change the partitioning behavior of trace elements into magnetite (Dare et al., 2015; Knipping et al., 2015b; Sievwright et al., 2017; Huang et al., 2019). The oscillatory zoning is widely distributed in MA and MB magnetite, suggesting that oscillatory zoning is not due to ultra-local fluid disequilibrium. The sharp compositional boundaries between the dark and light zones within single magnetite grains imply preservation of the original oscillatory zoning, which requires the growth rate of the crystal to be higher than intracrystalline diffusion (Watson and Liang, 1995). EPMA point analyses

498 indicate the trace element-rich zones (MA-IID, MB-ID, and dark bands in MA-III and
499 MB-II) involve all elements except V, and Ti for MA (Fig. 14), implying a relatively
500 high temperature and stable oxygen fugacity. Therefore, oscillatory zoning in
501 magnetite from MA and MB was likely probably caused by variation in temperature.

502 The rosette-like chlorite with similar oscillatory zoning was also observed from a
503 green-schist facies fault zone in Spain (Trincal et al., 2015). Previous studies showed
504 that chlorite chemistry can be a good indicator of the temperature of crystallization
505 (Cathelineau and Nieva 1985; Inoue et al. 2009; Bourdelle et al. 2013; Lanari et al.
506 2014). In this study, we use thermodynamic thermometer calibration of Lanari et al.
507 (2014) based on the following equilibrium: 2 clinochlore + 3 sudoite = 4 amesite + 4
508 H_2O + 7 quartz. The ideal contributions of amesite, clinochlore, and sudoite are
509 calculated using a site mixing model for chlorite end-members, and the ln(K) can be
510 calculated using the following equation: $\ln(K) = \ln(a^4\text{Ame} / a^2\text{Clna}^3\text{Sud})$. Chlorite
511 temperatures were then calculated using: T_{Chl} (ºC) = 172341 /[–Rln(K) + 315.149] –
512 273.15. The average calculated temperature of the dark and light band was 243 ºC and
513 444 ºC in zone 1, and 430 ºC and 212 ºC in zone 2, which were consistent with the
514 estimated temperature range of MA-III and MB-II magnetite (Fig. 13).

515 Texture features of MB magnetite reveal that the primary MB-I underwent a
516 process of dissolution and precipitation according to the sharp boundaries with
517 secondary magnetite, and the chlorite inclusions near the boundaries reveal that it
518 occurred in a lower temperature than primary magnetite (Fig. 6a). Moreover, some

519 MB-II magnetite also overgrows with primary MB-I grains (Fig. 5d), and these
520 overgrowing MB-II magnetite usually have oscillatory zoning (Fig. 5d). It is
521 reasonable to speculate that MB-II magnetite precipitated in two processes, including
522 the early dissolution of massive MB-I magnetite, and subsequent precipitation of
523 MB-II by two forms. For the coexisting chlorite, the zone 2 was synchronously
524 formed with the MB-II magnetite overgrowing with the MB-I grains, and the zone 1
525 most likely formed during the early dissolution of MB-I magnetite. Previous studies
526 have shown that increasing temperature, increasing chloride concentration, or
527 decreasing pH are the most important controls on the dissolution of magnetite because
528 these can enhance the solubility and the undersaturation of iron (Crerar et al., 1978;
529 Hemley and Hunt, 1992). Experimental studies also revealed that additions of HCl
530 could strongly enhance the solubility of magnetite in hydrothermal fluid (Holser and
531 Schneer, 1961; Chou and Eugster, 1977). External fluids such as basin brines or
532 formation waters that dissolved evaporites, which will increase the salinity and Cl
533 contents in ore-forming fluids, promoting the dissolution and reprecipitation process,
534 have been identified as important components in many Fe skarn and IOCG deposits
535 (Broughm et al., 2017; Bain et al., 2020; Hu et al., 2014; Huang and Beaudoin, 2019).
536 Therefore, the fluid composition especially the Cl content in equilibrium with MB-I
537 magnetite could have changed, causing the dissolution of MB-I magnetite. Combined
538 with the temperature variation in zone 1 of chlorite, it may indicate the incursion of
539 low-temperature external fluid which caused the change of fluid composition. The

composition of MB-II magnetite and chlorite, such as the higher Ti content in dark bands in MB-II magnetite (Fig. 14), and the decreasing of temperature from dark band to light band in zone 2 of chlorite, all indicate that the decreasing of temperature in fluid may result in the precipitation of MB-II magnetite.

IMPLICATIONS

At Shuanglong, the MA-I magnetite represents a transformational mushketovite phase characterized by abundant porosity and extremely high W content, which mainly display as micro- and invisible scheelite inclusions probably caused by the W expulsion during mushketovitization. The sharp contacts between primary dark magnetite and later light magnetite, suggest that they may have formed via coupled dissolution and reprecipitation. Moreover, the synchronous oscillatory zoning in light magnetite and coexisting chlorite was related to the variation of fluids temperature, and probably caused by the incursion of external low temperature and high salinity fluids which can dissolve the primary dark magnetite.

ACKNOWLEDGEMENTS

Our special thanks go to Peijun Lin and Haoran Dou for assisting with the EPMA analysis, and Fangyue Wang for assisting with the LA-ICP-MS analysis. Pete Hollings is thanked for comments on an early version of the paper. This work was supported by the National Natural Science Foundation of China (41725009, 42002083), and the Guangdong Major Project of Basic and Applied Basic Research

560 (2019B03032013) and Science and Technology planning project of Guangdong
561 Province (2017B030314175).

REFERENCES CITED

Bartlett, M. S. (1937) Properties of sufficiency and statistical tests. Proceedings of the Royal Society of London. Series A-Mathematical and Physical Sciences, 160(901), 268-282.

Bastrakov, E.N., Skirrow, R.G., and Davidson, G.J. (2007) Fluid Evolution and Origins of Iron Oxide Cu-Au Prospects in the Olympic Dam District, Gawler Craton, South Australia. Economic Geology, 102(8), 1415-1440.

Bain, W. M., Steele-MacInnis, M., Tornos, F., Hanchar, J. M., Creaser, E. C., & Pietruszka, D. K. (2021) Evidence for iron-rich sulfate melt during magnetite (-apatite) mineralization at El Laco, Chile. Geology.

Benavides, J., Kyser, T., Clark, A.H., Oates, C.J., Zamora, R., Tarnovschi, R., and Castillo, B. (2007) The Mantoverde iron oxide-copper-gold district, III Región, Chile: the role of regionally derived, nonmagmatic fluids in chalcopyrite mineralization. Economic Geology, 102(3), 415-440.

Bourdelle, F., Parra, T., Chopin, C., & Beyssac, O. (2013) A new chlorite geothermometer for diagenetic to low-grade metamorphic conditions. Contributions to Mineralogy and Petrology, 165(4), 723-735.

Broughm, S. G., Hanchar, J. M., Tornos, F., Westhues, A., & Attersley, S. (2017) Mineral chemistry of magnetite from magnetite-apatite mineralization and their host rocks: examples from Kiruna, Sweden, and El Laco, Chile. Mineralium Deposita, 52(8), 1223-1244.

583 Cathelineau, M., & Nieva, D. (1985) A chlorite solid solution geothermometer the Los
584 Azufres (Mexico) geothermal system. Contributions to Mineralogy and Petrology,
585 91(3), 235-244.
586 Canil, D., and Lacourse, T. (2020) Geothermometry using minor and trace elements in
587 igneous and hydrothermal magnetite. Chemical Geology, 541, 119576.
588 Chen, H., Clark, A.H., Kyser, T.K., Ullrich, T.D., Baxter, R., Chen, Y., and Moody, T.C.
589 (2010) Evolution of the Giant Marcona-Mina Justa Iron Oxide-Copper-Gold
590 District, South-Central Peru. Economic Geology, 105(1), 155-185.
591 Chen, H., Kyser, T.K., and Clark, A.H. (2011) Contrasting fluids and reservoirs in the
592 contiguous Marcona and Mina Justa iron oxide–Cu (–Ag–Au) deposits,
593 south-central Perú. Mineralium Deposita, 46(7), 677-706.
594 Chen, Z., Xiao, W., Windley, B.F., Schulmann, K., Mao, Q., Zhang, Z., Zhang, J.e.,
595 Deng, C., and Song, S. (2019) Composition, Provenance, and Tectonic Setting of
596 the Southern Kangurtag Accretionary Complex in the Eastern Tianshan, NW
597 China: Implications for the Late Paleozoic Evolution of the North Tianshan Ocean.
598 Tectonics.
599 Carew, M. J. (2004) Controls on Cu-Au mineralisation and Fe oxide metasomatism in
600 the Eastern fold belt, NW Queensland, Australia (Doctoral dissertation, James
601 Cook University).
602 Ciobanu, C.L., Wade, B.P., Cook, N.J., Schmidt Mumm, A., and Giles, D. (2013)
603 Uranium-bearing hematite from the Olympic Dam Cu–U–Au deposit, South

604 Australia: A geochemical tracer and reconnaissance Pb–Pb geochronometer.
605 Precambrian Research, 238, 129-147.
606 Crerar, D.A., Susak, N.J., Borcsik, M., and Schwartz, S. (1978) Solubility of the buffer
607 assemblage pyrite + pyrrhotite + magnetite in NaCl solutions from 200 to 350°C.
608 Geochimica et Cosmochimica Acta, 42(9), 1427-1437.
609 Corriveau, L., Montreuil, J. F., & Potter, E. G. (2016) Alteration facies linkages among
610 iron oxide copper-gold, iron oxide-apatite, and affiliated deposits in the Great Bear
611 magmatic zone, Northwest Territories, Canada. Economic Geology, 111(8),
612 2045-2072.
613 Cygan, G. L., & Candela, P. A. (1995) Preliminary study of gold partitioning among
614 pyrrhotite, pyrite, magnetite, and chalcopyrite at 600 to 700 (C, 140 MPa (1400
615 bars). In Thompson, JFH (ed.) Magmas, Fluids and Ore Deposits. Mineralogical
616 Association of Canada Short Course, 23, 129-37.
617 Dare, S.A., Barnes, S.-J., and Beaudoin, G. (2012) Variation in trace element content of
618 magnetite crystallized from a fractionating sulfide liquid, Sudbury, Canada:
619 implications for provenance discrimination. Geochimica et Cosmochimica Acta,
620 88, 27-50.
621 Dare, S.A., Barnes, S.-J., Beaudoin, G., Méric, J., Boutroy, E., and Potvin-Doucet, C.
622 (2014) Trace elements in magnetite as petrogenetic indicators. Mineralium
623 Deposita, 49(7), 785-796.
624 Deditius, A.P., Reich, M., Simon, A.C., Suvorova, A., Knipping, J., Roberts, M.P.,

625 Rubanov, S., Dodd, A., and Saunders, M. (2018) Nanogeochemistry of
626 hydrothermal magnetite. Contributions to Mineralogy & Petrology, 173(6), 46.
627 Dupuis, C., and Beaudoin, G. (2011) Discriminant diagrams for iron oxide trace
628 element fingerprinting of mineral deposit types. Mineralium Deposita, 46(4),
629 319-335.
630 Fleet, M. E., Crocket, J. H., & Stone, W. E. (1996) Partitioning of platinum-group
631 elements (Os, Ir, Ru, Pt, Pd) and gold between sulfide liquid and basalt melt.
632 Geochimica et Cosmochimica Acta, 60(13), 2397-2412.
633 Frost, B.R., 1991. Magnetic petrology: factors that control the occurrence of magnetite
634 in crustal rocks. In: Lindsley, D.H. (Ed.), Oxide Minerals: Petrologic and
635 Magnetic Significance. Rev. Mineral. Mineral. Soc. Am., pp. 489–509.
636 Ghiorso, M. S., & Sack, O. (1991) Fe-Ti oxide geothermometry: thermodynamic
637 formulation and the estimation of intensive variables in silicic magmas.
638 Contributions to Mineralogy and Petrology, 108(4), 485-510.
639 Han, Y.G., and Zhao, G.C. (2018) Final amalgamation of the Tianshan and Junggar
640 orogenic collage in the southwestern Central Asian Orogenic Belt: Constraints on
641 the closure of the Paleo-Asian Ocean. Earth-Science Reviews, 186, 129-152.
642 Hemley, J., Cygan, G., Fein, J., Robinson, G., and d'Angelo, W. (1992) Hydrothermal
643 ore-forming processes in the light of studies in rock-buffered systems; I,
644 Iron-copper-zinc-lead sulfide solubility relations. Economic Geology, 87(1), 1-22.
645 Holser, W. T., & Schneer, C. J. (1961) Hydrothermal magnetite. Geological Society of

America Bulletin, 72(3), 369-385.

Hu, H., Lentz, D., Li, J.-W., McCarron, T., Zhao, X.-F., and Hall, D. (2015) Reequilibration processes in magnetite from iron skarn deposits. Economic Geology, 110(1), 1-8.

Hu, H., Li, J.W., Lentz, D., Ren, Z., Zhao, X.F., Deng, X.D., and Hall, D. (2014) Dissolution–reprecipitation process of magnetite from the Chengchao iron deposit: Insights into ore genesis and implication for in-situ chemical analysis of magnetite. Ore Geology Reviews, 57(1), 393-405.

Hu, X., Chen, H., Beaudoin, G., and Zhang, Y. (2020) Textural and compositional evolution of iron oxides at Mina Justa (Peru): Implications for mushketovite and formation of IOCG deposits. American Mineralogist, 105(3), 397-408.

Hu, X., Chen, H., Zhao, L., Han, J., and Xia, X. (2017) Magnetite geochemistry of the Longqiao and Tieshan Fe–(Cu) deposits in the Middle-Lower Yangtze River Belt: Implications for deposit type and ore genesis. Ore Geology Reviews, 89, 822-835.

Huang, X.-W., and Beaudoin, G. (2019) Textures and Chemical Compositions of Magnetite from Iron Oxide Copper-Gold (IOCG) and Kiruna-Type Iron Oxide-Apatite (IOA) Deposits and Their Implications for Ore Genesis and Magnetite Classification Schemes. Economic Geology, 114(5), 953-979.

Huang, X.-W., Boutroy, É., Makvandi, S., Beaudoin, G., Corriveau, L., and De Toni, A.F. (2019a) Trace element composition of iron oxides from IOCG and IOA deposits: relationship to hydrothermal alteration and deposit subtypes.

667 Mineralium Deposita, 54(4), 525-552.

668 Huang, X.-W., Sappin, A.-A., Boutroy, É., Beaudoin, G., and Makvandi, S. (2019b)
669 Trace Element Composition of Igneous and Hydrothermal Magnetite from
670 Porphyry Deposits: Relationship to Deposit Subtypes and Magmatic Affinity.
671 Economic Geology, 114(5), 917-952.

672 Huang, X.-W., Zhou, M.-F., Beaudoin, G., Gao, J.-F., Qi, L., and Lyu, C. (2018) Origin
673 of the volcanic-hosted Yamansu Fe deposit, Eastern Tianshan, NW China:
674 constraints from pyrite Re-Os isotopes, stable isotopes, and in situ magnetite trace
675 elements. Mineralium Deposita, 53(7), 1039-1060.

676 Ilton, E.S., and Eugster, H.P. (1989) Base metal exchange between magnetite and a
677 chloride-rich hydrothermal fluid. Geochimica et Cosmochimica Acta, 53(2),
678 291-301.

679 Inoue, A., Meunier, A., Patrier-Mas, P., Rigault, C., Beaufort, D., & Vieillard, P. (2009)
680 Application of chemical geothermometry to low-temperature trioctahedral
681 chlorites. Clays and Clay Minerals, 57(3), 371-382.

682 Jiang, H., Han, J., Chen, H., Zheng, Y., Zhang, W., Lu, W., Deng, G., and Tan, Z. (2018)
683 Hydrothermal alteration, fluid inclusions and stable isotope characteristics of the
684 Shaquanzi Fe–Cu deposit, Eastern Tianshan: Implications for deposit type and
685 metallogenesis. Ore Geology Reviews, 100, 385-400.

686 Kaiser, H. F. (1958) The varimax criterion for analytic rotation in factor analysis.
687 Psychometrika, 23(3), 187-200.

688 Knipping, J.L., Bilenker, L.D., Simon, A.C., Reich, M., Barra, F., Deditius, A.P., Wälle,
689 M., Heinrich, C.A., Holtz, F., and Munizaga, R. (2015) Trace elements in
690 magnetite from massive iron oxide-apatite deposits indicate a combined formation
691 by igneous and magmatic-hydrothermal processes. Geochimica et Cosmochimica
692 Acta, 171, 15-38.
693 Lanari, P., Wagner, T., & Vidal, O. (2014) A thermodynamic model for di-trioctahedral
694 chlorite from experimental and natural data in the system MgO–FeO–Al_2O_3–
695 SiO_2–H_2O: applications to P–T sections and geothermometry. Contributions to
696 Mineralogy and Petrology, 167(2), 968.
697 Lindsley, D. H., and Frost, B. R. (1991) Equilibria among Fe-Ti oxides, pyroxenes,
698 olivine, and quartz: Part I. Theory. American Mineralogist, 77(9-10), 987-1003.
699 Liang, P., Wu, C., Hu, X., and Xie, Y. (2020) Textures and geochemistry of magnetite:
700 Indications for genesis of the Late Paleozoic Laoshankou Fe-Cu-Au deposit, NW
701 China. Ore Geology Reviews, 124, 103632.
702 Liu, Y., Hu, Z., Gao, S., Günther, D., Xu, J., Gao, C., and Chen, H. (2008) In situ
703 analysis of major and trace elements of anhydrous minerals by LA-ICP-MS
704 without applying an internal standard. Chemical Geology, 257(1-2), 34-43.
705 Marschik, R., & Fontboté, L. (2001) The Candelaria-Punta del Cobre iron oxide Cu-Au
706 (-Zn-Ag) deposits, Chile. Economic Geology, 96(8), 1799-1826.
707 Mao, J., Goldfarb, R.J., Wang, Y., Hart, C.J., Wang, Z., and Yang, J. (2005) Late
708 Paleozoic base and precious metal deposits, East Tianshan, Xin-jiang, China:

709 Characteristics and geodynamic setting. Episodes-Newsmagazine of the
710 International Union of Geological Sciences, 28(1), 23-30.

711 McIntire, W. (1963) Trace element partition coefficients—a review of theory and
712 applications to geology. Geochimica et Cosmochimica Acta, 27(12), 1209-1264.

713 Mücke, A., & Cabral, A. R. (2005) Redox and nonredox reactions of magnetite and
714 hematite in rocks. Geochemistry, 65(3), 271-278.

715 Nadoll, P., Angerer, T., Mauk, J.L., French, D., and Walshe, J. (2014) The chemistry of
716 hydrothermal magnetite: a review. Ore geology reviews, 61, 1-32.

717 Nadoll, P., Mauk, J.L., Hayes, T.S., Koenig, A.E., and Box, S.E. (2012) Geochemistry
718 of magnetite from hydrothermal ore deposits and host rocks of the
719 Mesoproterozoic Belt Supergroup, United States. Economic Geology, 107(6),
720 1275-1292.

721 Nielsen, R. L., Forsythe, L. M., Gallahan, W. E., & Fisk, M. R. (1994) Major-and
722 trace-element magnetite-melt equilibria. Chemical Geology, 117(1-4), 167-191.

723 Ning, S., Wang, F., Xue, W., and Zhou, T. (2017) Geochemistry of the Baoshan pluton
724 in the Tongling region of the Lower Yangtze River Belt. Geochimica, 46(5),
725 397-412.

726 Ohmoto, H. (2003) Nonredox transformations of magnetite-hematite in hydrothermal
727 systems. Economic Geology, 98(1), 157-161.

728 Qin, K.-z., Su, B.-x., Sakyi, P.A., Tang, D.-m., Li, X.-h., Sun, H., Xiao, Q.-h., and Liu,
729 P.-p. (2011) SIMS zircon U-Pb geochronology and Sr-Nd isotopes of

730 Ni-Cu-Bearing Mafic-Ultramafic Intrusions in Eastern Tianshan and Beishan in
731 correlation with flood basalts in Tarim Basin (NW China): Constraints on a ca. 280
732 Ma mantle plume. American Journal of Science, 311(3), 237-260.
733 Righter, K., Leeman, W., and Hervig, R. (2006) Partitioning of Ni, Co and V between
734 spinel-structured oxides and silicate melts: Importance of spinel composition.
735 Chemical Geology, 227(1-2), 1-25.
736 Sengor, A. (1996) Paleotectonics of Asia: fragments of a synthesis. The tectonic
737 evolution of Asia, 486-640.
738 Sengor, A.M.C., Natalin, B., and Burtman, V. (1993) Evolution of the Altaid Tectonic
739 collage and Palaeozoic Crustal Growth in Eurasia. Nature, 364.
740 Sievwright, R. H., Wilkinson, J. J., O'Neill, H. S. C., & Berry, A. J. (2017)
741 Thermodynamic controls on element partitioning between titanomagnetite and
742 andesitic–dacitic silicate melts. Contributions to Mineralogy and Petrology,
743 172(8), 1-33.
744 Simon, A. C., Pettke, T., Candela, P. A., Piccoli, P. M., & Heinrich, C. A. (2004)
745 Magnetite solubility and iron transport in magmatic-hydrothermal environments.
746 Geochimica et Cosmochimica Acta, 68(23), 4905-4914.
747 Simon, A. C., Candela, P. A., Piccoli, P. M., Mengason, M., & Englander, L. (2008) The
748 effect of crystal-melt partitioning on the budgets of Cu, Au, and Ag. American
749 Mineralogist, 93(8-9), 1437-1448.
750 Trincal, V., Lanari, P., Buatier, M., Lacroix, B., Charpentier, D., Labaume, P., & Muñoz,

751 M. (2015) Temperature micro-mapping in oscillatory-zoned chlorite: Application
752 to study of a green-schist facies fault zone in the Pyrenean Axial Zone (Spain).
753 American Mineralogist, 100(11-12), 2468-2483.
754 Toplis, M. J., & Carroll, M. R. (1995) An experimental study of the influence of oxygen
755 fugacity on Fe-Ti oxide stability, phase relations, and mineral—melt equilibria in
756 ferro-basaltic systems. Journal of Petrology, 36(5), 1137-1170.
757 Toplis, M. J., & Corgne, A. (2002) An experimental study of element partitioning
758 between magnetite, clinopyroxene and iron-bearing silicate liquids with particular
759 emphasis on vanadium. Contributions to Mineralogy and Petrology, 144(1),
760 22-37.
761 Verdugo-Ihl, M.R., Ciobanu, C.L., Cook, N.J., Ehrig, K., Slattery, A., and
762 Courtney-Davies, L. (2020) Trace-element remobilisation from W–Sn–U–Pb
763 zoned hematite: Nanoscale insights into a mineral geochronometer behaviour
764 during interaction with fluids. Mineralogical Magazine, 84(4), 502-516.
765 Verdugo-Ihl, M.R., Ciobanu, C.L., Cook, N.J., Ehrig, K.J., Courtney-Davies, L., and
766 Gilbert, S. (2017) Textures and U-W-Sn-Mo signatures in hematite from the
767 Olympic Dam Cu-U-Au-Ag deposit, South Australia: Defining the archetype for
768 IOCG deposits. Ore Geology Reviews, 91, 173-195.
769 Watson, E. B., & Liang, Y. (1995) A simple model for sector zoning in slowly grown
770 crystals: Implications for growth rate and lattice diffusion, with emphasis on
771 accessory minerals in crustal rocks. American Mineralogist, 80(11-12),

1179-1187.

Wang, F., Gan, G., Siyuan, N., LiQing, N., GuoXiong, Z., and White, N.C. (2017) A new approach to LA-ICP-MS mapping and application in geology. Acta Petrologica Sinica, 33(11), 3422-3436.

Wen, G., Li, J.-W., Hofstra, A.H., Koenig, A.E., Lowers, H.A., and Adams, D. (2017) Hydrothermal reequilibration of igneous magnetite in altered granitic plutons and its implications for magnetite classification schemes: Insights from the Handan-Xingtai iron district, North China Craton. Geochimica et Cosmochimica Acta, 213, 255-270.

Whitney, J.A., Hemley, J.J., and Simon, F.O. (1985) The concentration of iron in chloride solutions equilibrated with synthetic granitic compositions; the sulfur-free system. Economic Geology, 80(2), 444-460.

Whalen, J. B., & Chappell, B. W. (1988) Opaque mineralogy and mafic mineral chemistry of I-and S-type granites of the Lachlan fold belt, southeast Australia. American Mineralogist, 73(3-4), 281-296.

Windley, B.F., Alexeiev, D., Xiao, W.J., Kroner, A., and Badarch, G. (2007) Tectonic models for accretion of the Central Asian Orogenic Belt. Journal of the Geological Society, 164, 31-47.

Wood, S. A., & Samson, I. M. (2000) The hydrothermal geochemistry of tungsten in granitoid environments: I. Relative solubilities of ferberite and scheelite as a function of T, P, pH, and m NaCl. Economic Geology, 95(1), 143-182.

Wu, C., Chen, H., Hong, W., Li, D., Liang, P., Fang, J., Zhang, L., and Lai, C. (2019) Magnetite chemistry and implications for the magmatic-hydrothermal ore-forming process: An example from the Devonian Yuleken porphyry Cu system, NW China. Chemical Geology, 522, 1-15.

Xiao, W.J., Windley, B.F., Allen, M.B., and Han, C.M. (2013) Paleozoic multiple accretionary and collisional tectonics of the Chinese Tianshan orogenic collage. Gondwana Research, 23(4), 1316-1341.

Xiao, W.J., Zhang, L.C., Qin, K.Z., Sun, S., and Li, J.L. (2004) Paleozoic accretionary and collisional tectonics of the Eastern Tianshan (China): Implications for the continental growth of Central Asia. American Journal of Science, 304(4), 370-395.

Xinjiang Uygur Autonomous Region Geological Survey (abv. XUARGS). (2003) Report for Target Selection and Potential Resources in Caixiashan–Jintan in the Eastern Tianshan, Xinjiang. pp. 1–187 (in Chinese).

Zhang, S., Chen, H., Hollings, P., Zhao, L., and Gong, L. (2020a) Tectonic and magmatic evolution of the Aqishan-Yamansu belt: A Paleozoic arc-related basin in the Eastern Tianshan (NW China). GSA Bulletin.

Zhang, W., Chen, H., Peng, L., Zhao, L., Huang, J., Lu, W., Liang, P., and Lai, C. (2018a) Discriminating hydrothermal fluid sources using tourmaline boron isotopes: Example from Bailingshan Fe deposit in the Eastern Tianshan, NW China. Ore Geology Reviews, 98, 28-37.

814 Zhang, W., Chen, H., Peng, L., Zhao, L., Lu, W., Zhang, Z., Yang, J., and Sun, J. (2018b)
815 Ore genesis of the Duotoushan Fe-Cu deposit, Eastern Tianshan, NW China:
816 Constraints from ore geology, mineral geochemistry, fluid inclusion and stable
817 isotopes. Ore Geology Reviews, 100, 401-421.
818 Zhang, Y., Hollings, P., Shao, Y., Li, D., Chen, H., and Li, H. (2020b) Magnetite texture
819 and trace-element geochemistry fingerprint of pulsed mineralization in the
820 Xinqiao Cu-Fe-Au deposit, Eastern China. American Mineralogist, 105(11),
821 1712-1723.
822 Zhao, L., Chen, H., Hollings, P., and Han, J. (2019) Late Paleozoic magmatism and
823 metallogenesis in the Aqishan-Yamansu belt, Eastern Tianshan: Constraints from
824 the Bailingshan intrusive complex. Gondwana Research, 65, 68-85.
825 Zhao, L., Chen, H., Zhang, L., Li, D., Zhang, W., Wang, C., Yang, J., and Yan, X.
826 (2018a) Magnetite geochemistry of the Heijianshan Fe–Cu (–Au) deposit in
827 Eastern Tianshan: Metallogenic implications for submarine volcanic-hosted Fe–
828 Cu deposits in NW China. Ore Geology Reviews, 100, 422-440.
829 Zhao, L., Chen, H., Zhang, L., Xia, X., Zhang, W., Li, D., Lu, W., Liang, P., Li, R., Yang,
830 J., and Yan, X. (2017) Geology and ore genesis of the late Paleozoic Heijianshan
831 Fe oxide–Cu (–Au) deposit in the Eastern Tianshan, NW China. Ore Geology
832 Reviews, 91, 110-132.
833 Zhao, L., Chen, H., Zhang, L., Zhang, W., Yang, J.T., and Yan, X.L. (2018b) The Late
834 Paleozoic magmatic evolution of the Aqishan-Yamansu belt, Eastern Tianshan:

Constraints from geochronology, geochemistry and Sr-Nd-Pb-Hf isotopes of igneous rocks. Journal of Asian Earth Sciences, 153, 170-192.

Zhou, T., Yuan, F., Zhang, D., Fan, Y., Liu, S., Peng, M., and Zhang, J. (2010) Geochronology, tectonic setting and mineralization of granitoids in Jueluotage area, eastern Tianshan, Xinjiang. Acta Petrologica Sinica, 26(2), 478-502 [in Chinese with English abstract].

Figure captions

Figure 1. (a) Simplified tectonic map of the Central Asian orogenic belt (CAOB), modified after Şengör (1996). (b) Tectonic map of north Xinjiang, modified after Chen et al. (2012). (c) Geological map of the Eastern Tianshan and distribution of the ore deposits, modified after Zhao et al. (2019).

Figure 2. Geological map of the Shuanglong Fe-Cu deposit (modified after Xinjiang Uygur Autonomous Region Geological Survey (2003)).

Figure 3. Alteration and mineralization paragenesis of the Shuanglong Fe–Cu deposit.

Figure 4. Photographs showing representative alteration/mineralization paragenesis in the Shuanglong Fe-Cu deposit. (**a**) platy MA magnetite. (**b**) photomicrographs of platy MA magnetite. (**c**) massive magnetite coexisting with amphibole, chlorite and chalcopyrite. (**d**) photomicrographs of massive MB magnetite. (**e**) MC magnetite coexisting with K-feldspar, epidote, and amphibole in host rock of the Tugutubulak Formation. (**f**) photomicrograph of granular MC magnetite coexisting with K-feldspar and epidote. (**g-h**) quartz-hematite-chalcopyrite vein cutting platy MA

855 magnetite. Abbreviations: *Mag* = magnetite, *Kfs* = potassium feldspar, *Cal* = calcite, *Ep* = epidote,
856 *Amp* = amphibole, *Qtz* = quartz, *Hem* = hematite, *Ccp* = chalcopyrite, *Chl* = chlorite.

857 **Figure 5.** Photomicrographs (**a, c, e, and g**) and BSE images (**b, d, f, and h**) of the Shuanglong
858 magnetite. (**a**) Platy magnetite (MA). (**b**) BSE images of platy magnetite, which shows three
859 different zones. MA-I magnetite is light with abundant porosity and inclusions. MA-II magnetite
860 is dark and shows chemical oscillatory zoning. And MA-III magnetite is light and lack of porosity
861 and inclusions. (**c**) massive magnetite (MB). (**d**) Two generations of magnetite in massive
862 magnetite (MB). The first generation of magnetite (MB-I) shows oscillatory zoning composed of
863 dark-gray (MB-ID) and light-gray (MB-IL) zones, and MB-ID magnetite was replaced by MB-IL
864 magnetite which contains abundant porosity and inclusions. The second generation of magnetite
865 (MB-II) crosscuts MB-I magnetite and contains porosity and inclusions locally. (**e**) Massive
866 magnetite (MB) and later mineral assemblage of chalcopyrite-sphalerite-chlorite. (**f**) BSE image of
867 MB magnetite shows that the secondary magnetite (MB-II) contains chalcopyrite inclusions
868 crosscuts the first generation of magnetite (MB-I). (**g**) Granular magnetite (MC) coexisting with
869 K-feldspar and epidote, and K-feldspar was replaced by late epidote and calcite. (**h**) BSE image of
870 MC magnetite, which shows two different zones. MC-I magnetite is dark and replaced by MC-II
871 light magnetite. Abbreviations: *Mag* = magnetite, *Kfs* = potassium feldspar, *Ep* = epidote, *Amp* =
872 amphibole, *Qtz* = quartz, *Hem* = hematite, *Chl* = chlorite, *Sch* = scheelite, *Ccp* = chalcopyrite, *Sp*
873 = sphalerite, *Cal* = calcite.

874 **Figure 6.** BSE images (**a and b**) of the MB magnetite and coexisting chlorite, and EMPA mapping
875 of selected elements in chlorite. Abbreviations: *Hem* = hematite, *Chl* = chlorite.

Figure 7. EMPA mapping of selected elements in magnetites from the Shuanglong deposit.

Figure 8. Box diagram of major (a) and trace (b) elements concentrations for the Shuanglong magnetite.

Figure 9. Rotated component plot for magnetite showing factor analysis results from trace elements with significant content.

Figure 10. Plots displaying negative correlations between (**a)** Si and Al vs. calculated Fe^{3+} in atom per formula unit (a.p.f.u.) and (**b)** Mg and Ca vs. Fe^{2+} (a.p.f.u.).

Figure 11. Time-resolved analytical signal of LA-ICP-MS analysis for MA-I magnetite. CPS = counts per second.

Figure 12. Binary diagrams of (**a**) Ga vs. Ti, (**b**) Zn vs. Ti, (**c**) Ni vs. V, (**d**) Cr vs. V, (**e**) Sc vs. V, (**f**) Sr vs. Al, (**g**) Sr vs. Ca and (**h**) W vs. Mn for the Shuanglong magnetite.

Figure 13. Plots of (Al + Mn) vs. (Ti + V) diagram, modified after Nadoll et al. (2014) and Deditius et al. (2018).

Figure 14. EPMA transects across the oscillatory zoning in dark and light magnetite.

Table 1. Mean, minimum, and maximum contents (wt%) of magnetite from the Shuanglong deposit by electron microprobe analyses

Magnetite type		Fe	Si	Al	Ca	Mg	Mn	Ti	V	Cr	Ni
MA-I (n=30)	Mean	72.868	0.025	0.018	0.033	0.008	0.084	0.031	0.018	0.015	b.d.l
	Min	70.019	b.d.l	b.d.l	b.d.l	b.d.l	b.d.l	b.d.l	b.d.l	b.d.l	b.d.l
	Max	73.711	0.097	0.037	0.090	0.011	0.154	0.037	0.020	0.023	b.d.l
MA-IID (n=29)	Mean	68.488	1.400	0.428	0.675	0.081	0.130	0.034	0.024	0.017	0.026
	Min	67.238	1.014	0.209	0.417	0.061	0.026	b.d.l	b.d.l	b.d.l	b.d.l
	Max	69.885	1.646	0.597	0.855	0.125	0.197	0.052	0.044	0.027	0.032
MA-IIL (n=21)	Mean	69.965	0.942	0.217	0.418	0.060	0.117	0.040	0.027	0.037	0.025
	Min	67.444	0.089	0.025	0.044	0.004	0.029	b.d.l	b.d.l	b.d.l	b.d.l
	Max	71.229	1.305	0.409	0.666	0.103	0.177	0.073	0.033	0.097	0.025
MA-III (n=36)	Mean	72.171	0.192	0.087	0.253	0.022	0.083	0.036	0.022	0.025	b.d.l
	Min	69.058	0.014	b.d.l	b.d.l	b.d.l	b.d.l	b.d.l	b.d.l	b.d.l	b.d.l
	Max	73.217	1.070	0.414	0.398	0.054	0.147	0.046	0.040	0.032	b.d.l
MB-ID (n=27)	Mean	68.763	1.072	0.518	0.560	0.068	0.072	0.112	0.024	0.023	b.d.l
	Min	67.133	0.850	0.343	0.404	0.034	b.d.l	0.061	0.015	b.d.l	b.d.l
	Max	69.990	1.447	0.677	0.748	0.159	0.132	0.187	0.034	0.040	b.d.l
MB-IL (n=11)	Mean	69.971	0.732	0.333	0.399	0.049	0.071	0.060	0.024	0.017	b.d.l
	Min	69.373	0.620	0.248	0.340	0.028	b.d.l	0.027	b.d.l	b.d.l	b.d.l
	Max	70.976	0.837	0.372	0.447	0.094	0.114	0.100	0.030	0.020	b.d.l
MB-II (n=17)	Mean	72.101	0.113	0.030	0.040	0.010	0.058	0.049	0.030	0.024	b.d.l
	Min	71.138	0.043	0.006	b.d.l	b.d.l	b.d.l	b.d.l	b.d.l	b.d.l	b.d.l
	Max	72.790	0.326	0.076	0.090	0.013	0.097	0.064	0.055	0.031	b.d.l
MC-I (n=13)	Mean	70.018	0.691	0.175	0.361	0.039	0.140	0.041	0.061	0.023	0.037
	Min	69.165	0.364	0.066	0.151	0.023	0.092	0.002	0.004	b.d.l	b.d.l
	Max	71.273	0.858	0.268	0.539	0.055	0.170	0.069	0.088	0.037	0.037
MC-II (n=18)	Mean	71.595	0.181	0.018	0.063	0.008	0.095	0.031	0.041	0.028	0.036
	Min	71.005	0.098	0.005	0.023	b.d.l	0.055	b.d.l	0.017	b.d.l	b.d.l
	Max	72.092	0.261	0.041	0.234	0.013	0.132	0.039	0.073	0.072	0.037

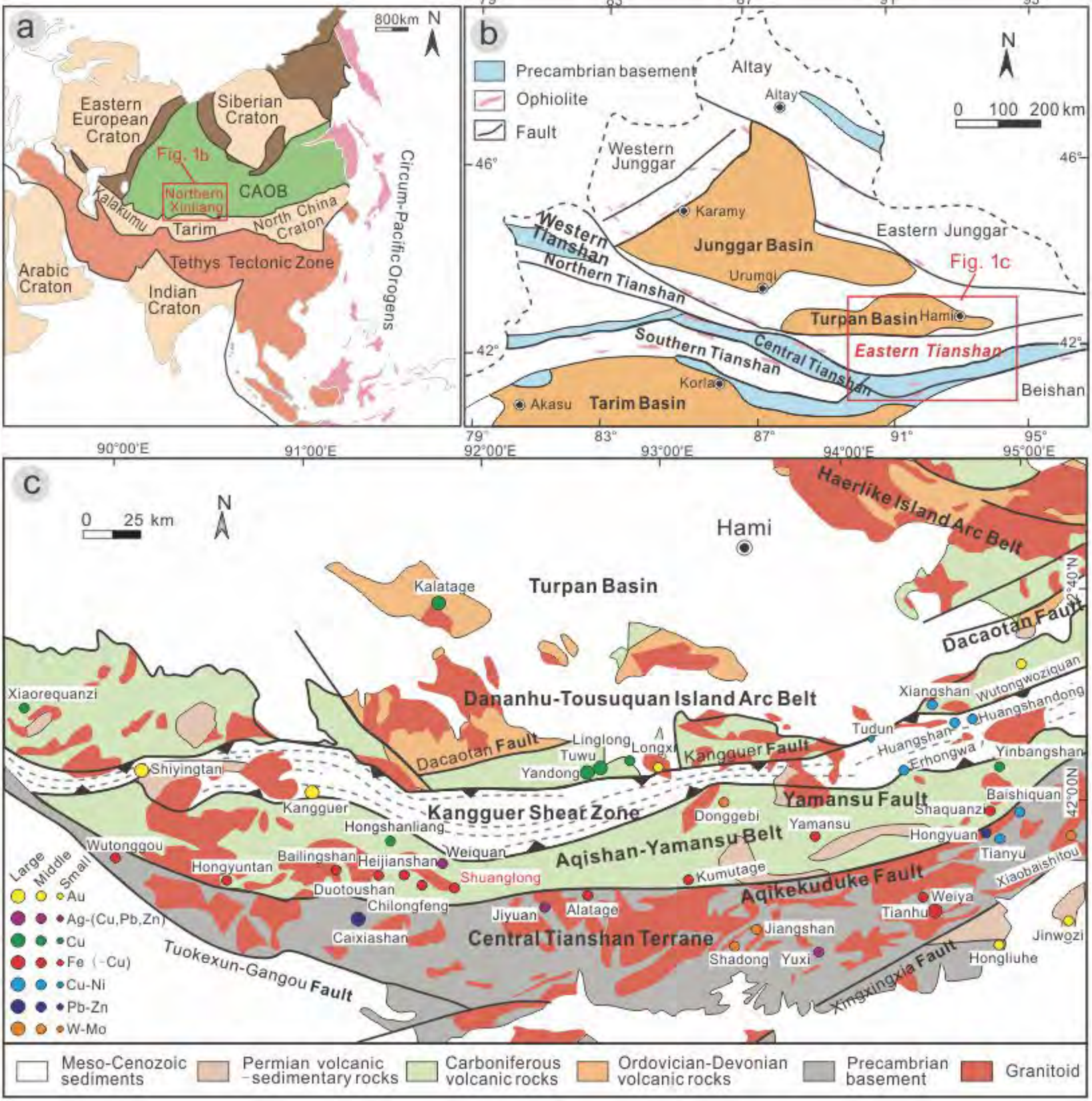
a
800km
N
Eastern European Craton
Siberian Craton
Fig. 1b
Northern Xinjiang
CAOB
Kalakumu
Tarim
North China Craton
Tethys Tectonic Zone
Arabic Craton
Indian Craton
Circum-Pacific Orogens
b
Precambrian basement
Ophiolite
Fault
Altay
Western Junggar
Karamy
Junggar Basin
Eastern Junggar
Western Tianshan
Northern Tianshan
Urumqi
Turpan Basin
Hami
Fig. 1c
Southern Tianshan
Central Tianshan
Eastern Tianshan
Beishan
Korla
Akasu
Tarim Basin
0 100 200 km
c
0 25 km
Hami
Haerlike Island Arc Belt
Turpan Basin
Kalatage
Dacaotan Fault
Dananhu-Tousuquan Island Arc Belt
Xiaorequanzi
Xiangshan
Wutongwoziquan
Huangshandong
Tudun
Huangshan
Erhongwa
Yinbangshan
Linglong
Tuwu
Yandong
Longxi
Kangguer Fault
Shiyingtan
Kangguer
Kangguer Sheat Zone
Yamansu Fault
Donggebi
Yamansu
Shaquanzi
Baishiquan
Hongshanliang
Aqishan-Yamansu Belt
Hongyuan
Tianyu
Wutonggou
Bailingshan
Heijianshan
Weiquan
Hongyuntan
Shuanglong
Duotoushan
Kumutage
Xiaobaishitou
Aqikekuduke Fault
Weiya
Tianhu
Chilongfeng
Jiyuan
Alatage
Caixiashan
Central Tianshan Terrane
Jiangshan
Jinwozi
Shadong
Yuxi
Hongliuhe
Tuokexun-Gangou Fault
Xingxingxia Fault
42°40'N
42°00'N
90°00'E
91°00'E
92°00'E
93°00'E
94°00'E
95°00'E
Large
Middle
Small
Au
Ag-(Cu,Pb,Zn)
Cu
Fe (-Cu)
Cu-Ni
Pb-Zn
W-Mo
Meso-Cenozoic sediments
Permian volcanic -sedimentary rocks
Carboniferous volcanic rocks
Ordovician-Devonian volcanic rocks
Precambrian basement
Granitoid

Fig 1

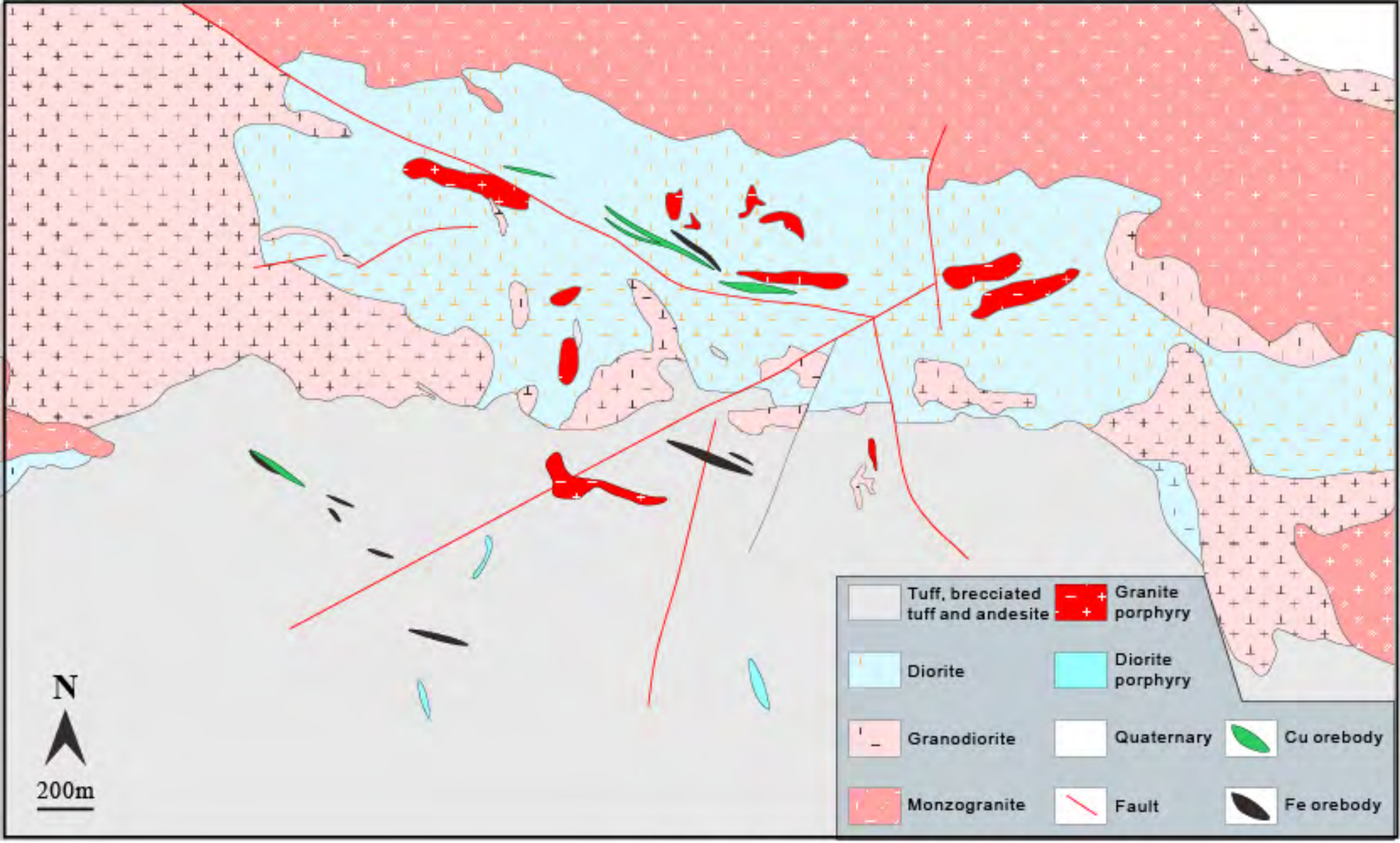
Tuff, brecciated tuff and andesite
Granite porphyry
Diorite
Diorite porphyry
Granodiorite
Quaternary
Cu orebody
Monzogranite
Fault
Fe orebody
N
200m

Fig 2

Minerals	Stage I skarn alternation	Stage II Fe mineralization	Stage III Cu mineralization
Garnet	———		
Hematite		———	———
Epidote		———	———
K-feldspar		———	
Amphibole		———	
Magnetite		———	———
Pyrite		———	———
Calcite		– – –	———
Apitate		– – –	
Quartz		———	———
Chlorite		———	———
Chalcopyrite		– – –	———
Gypsum			———
Galena			– – –
Bornite			– – –
Sphalerite			– – –

——— Abundant ——— Local – – – Trace

Fig 3

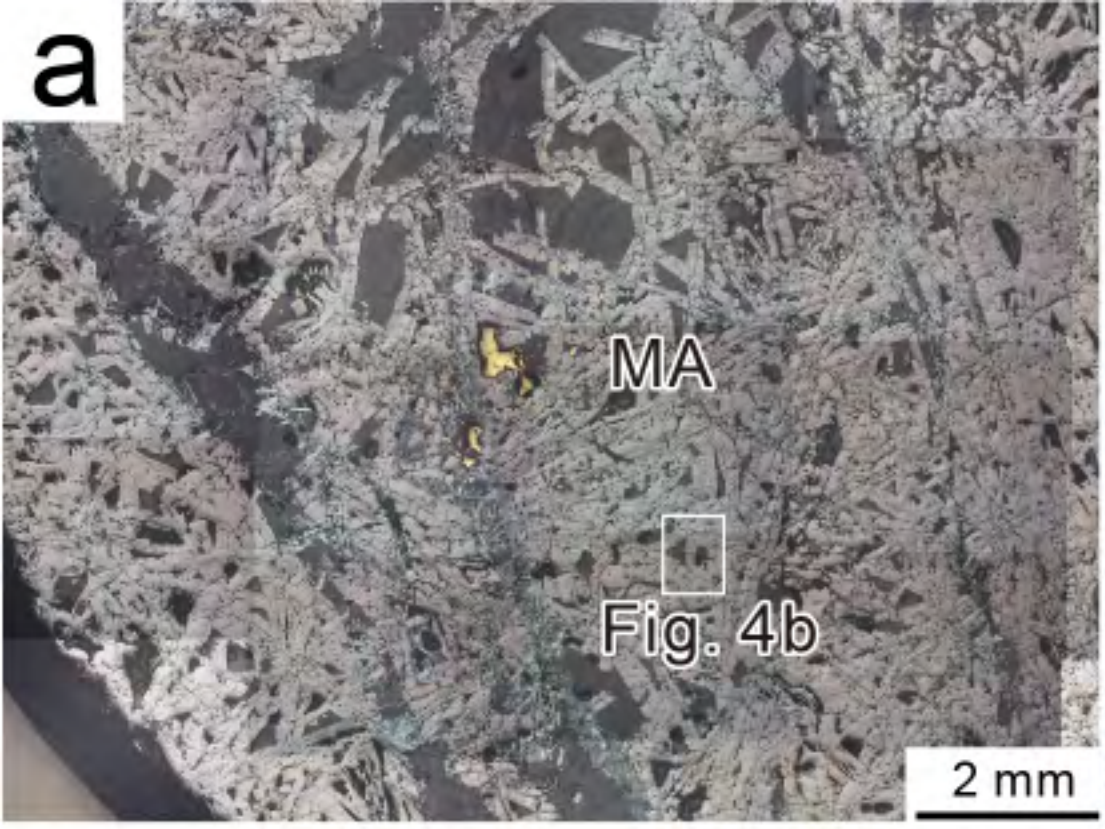
a
MA
Fig. 4b
2 mm

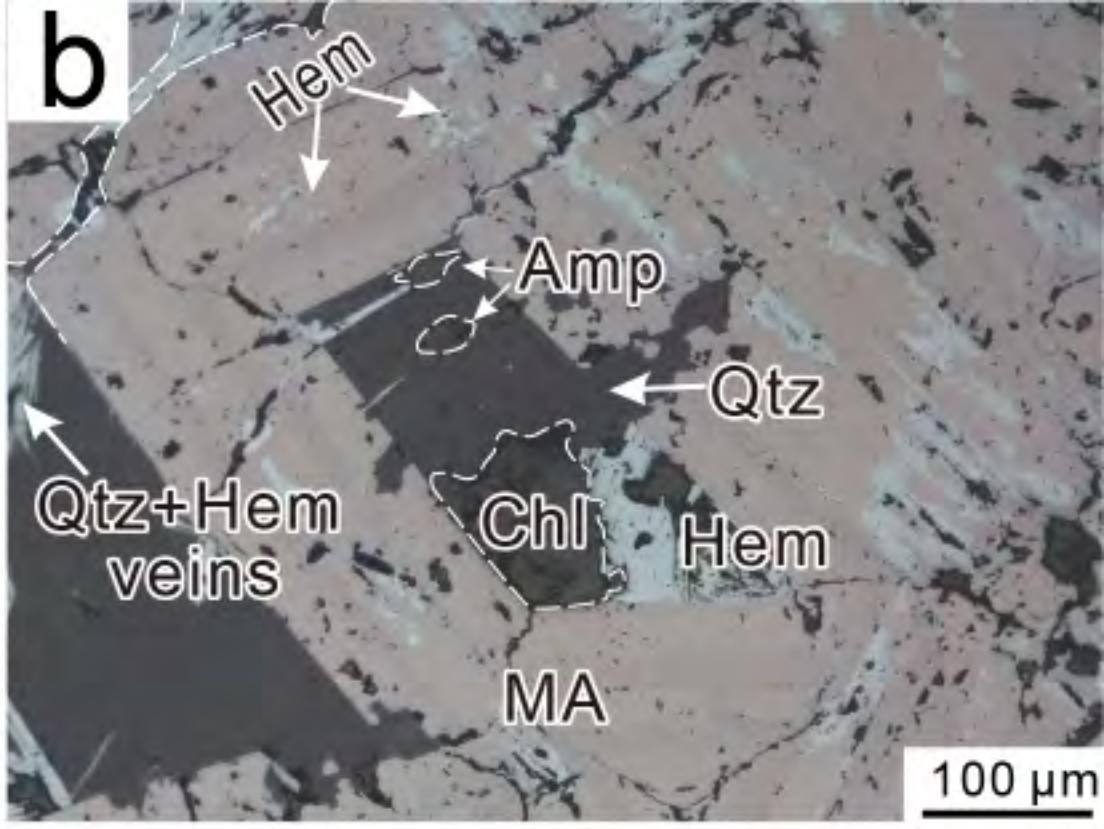
b
Hem
Amp
Qtz
Qtz+Hem
veins
Chl
Hem
MA
100 μm

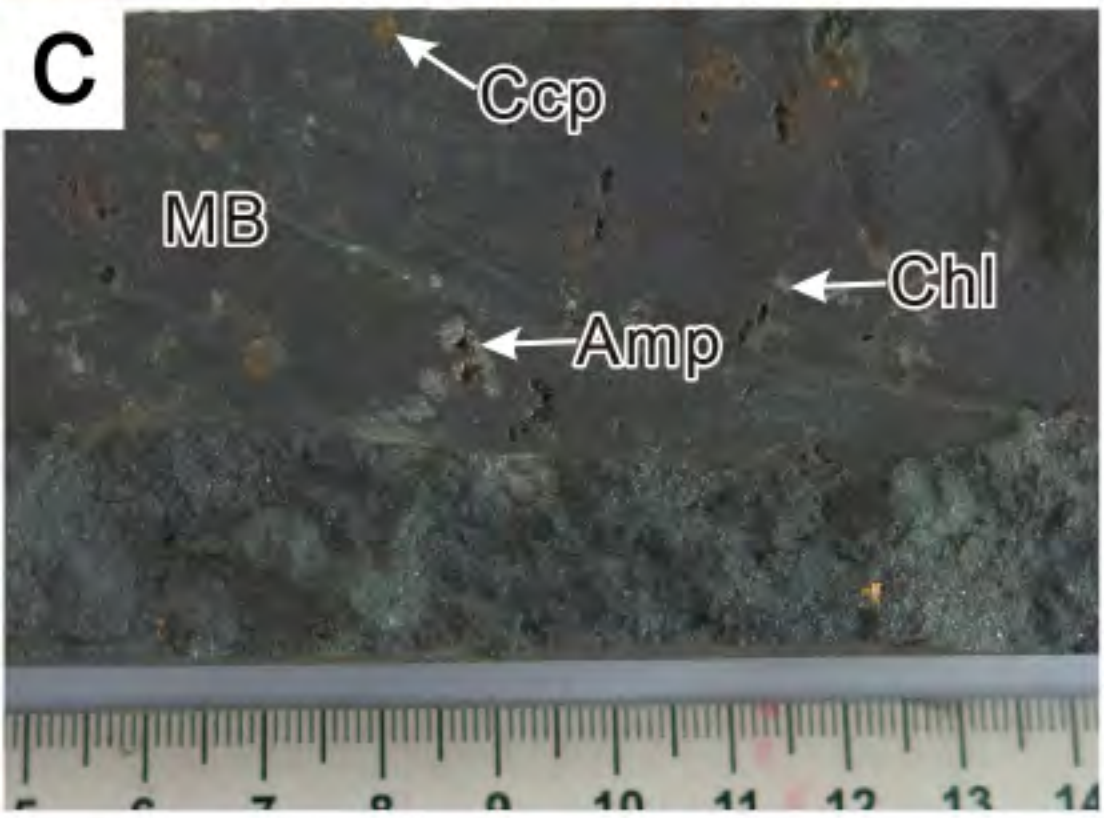
c
Ccp
MB
Chl
Amp

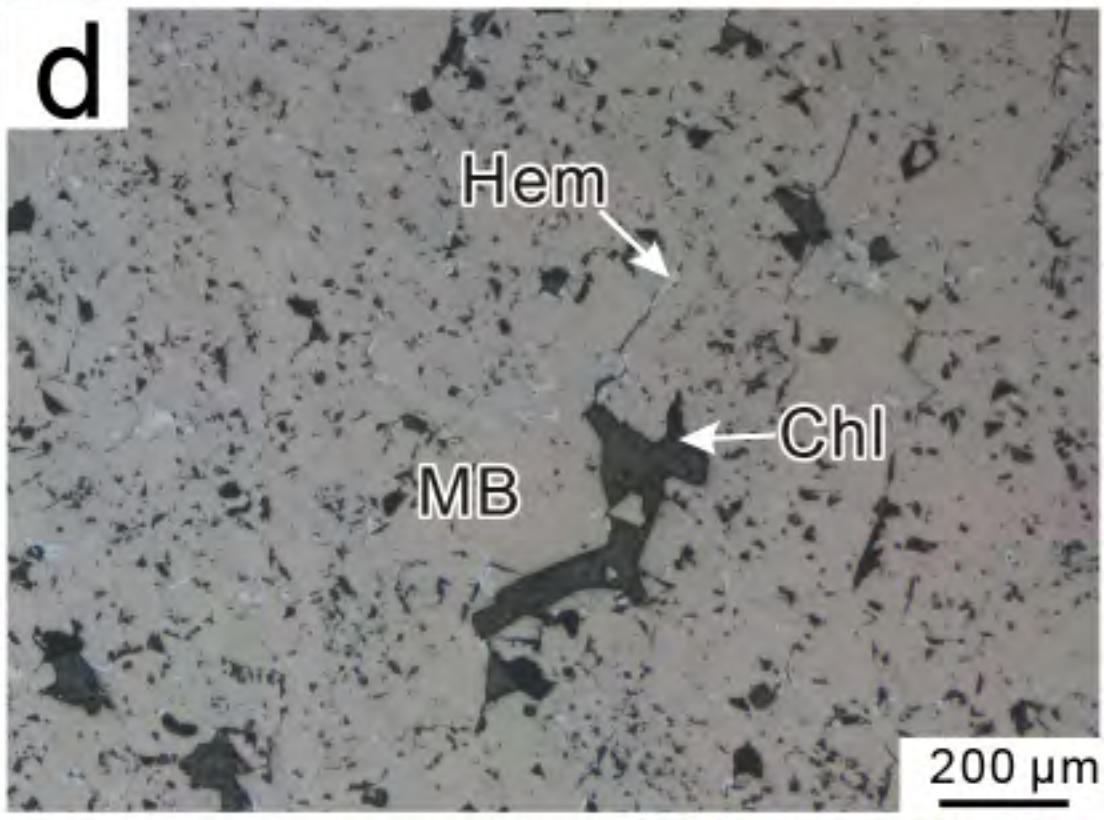
d
Hem
Chl
MB
200 μm

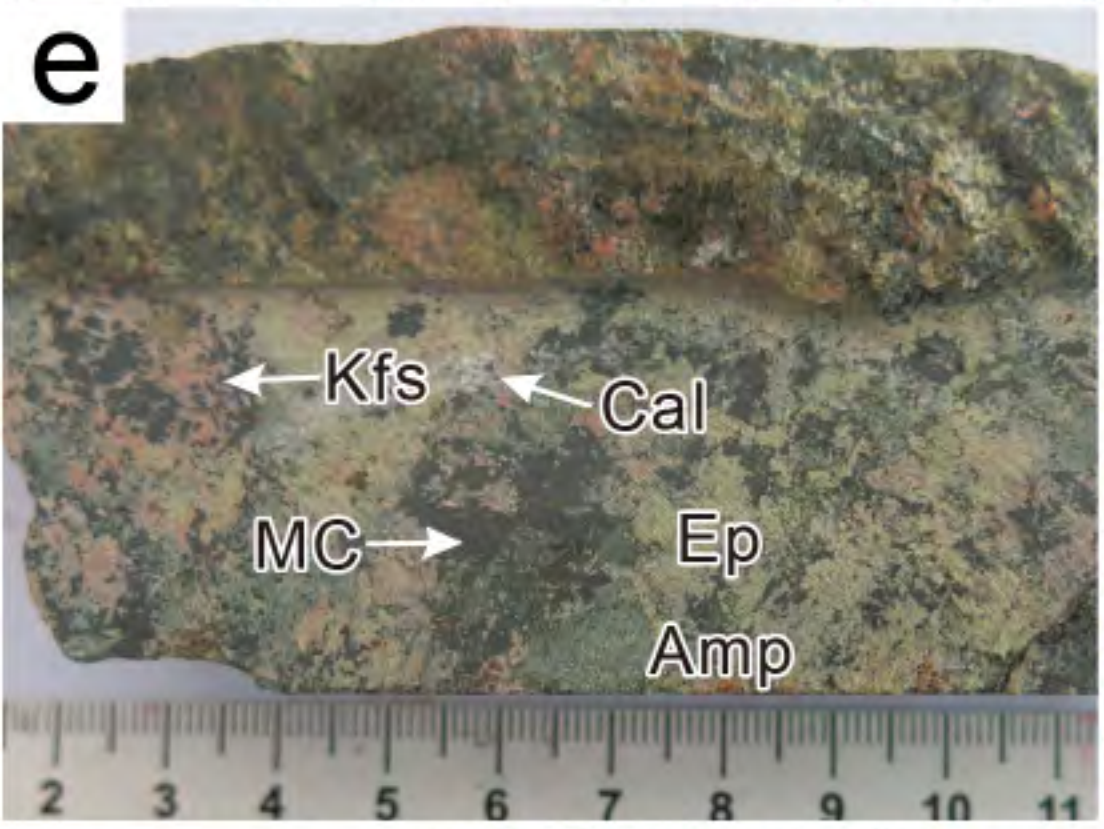
e
Kfs
Cal
MC
Ep
Amp

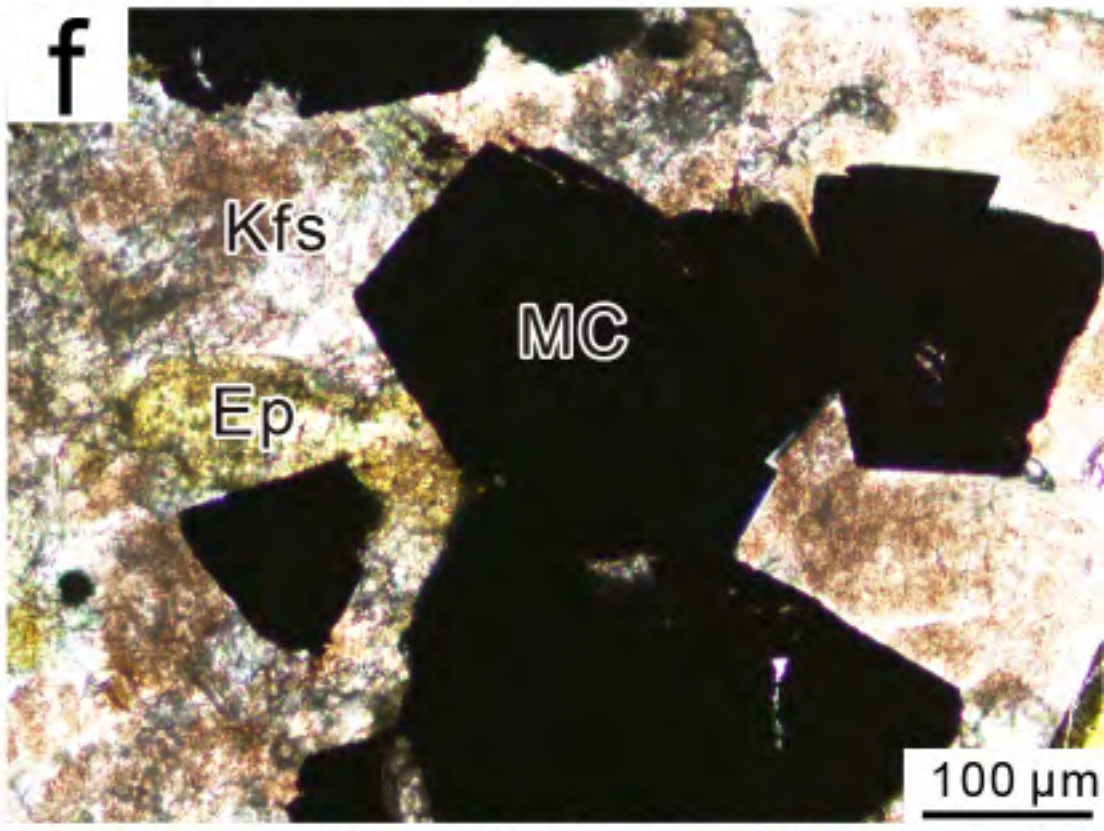
f
Kfs
MC
Ep
100 μm

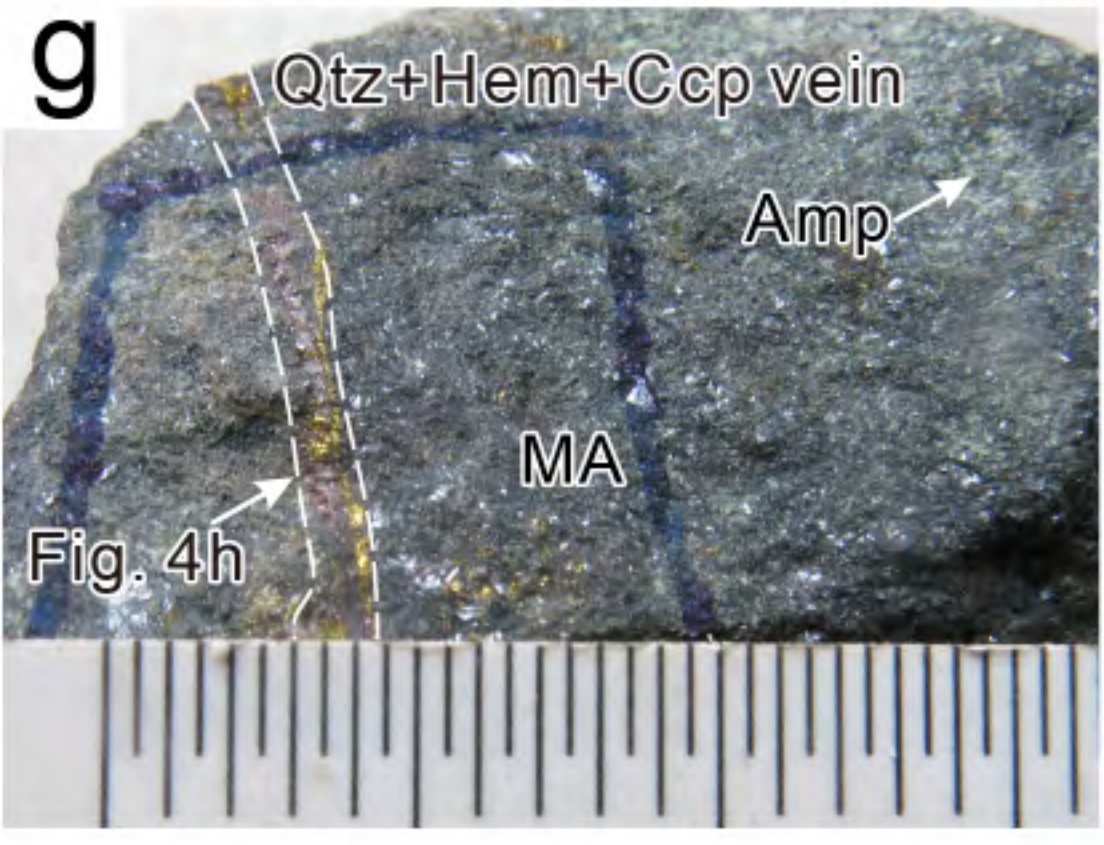
g
Qtz+Hem+Ccp vein
Amp
MA
Fig. 4h

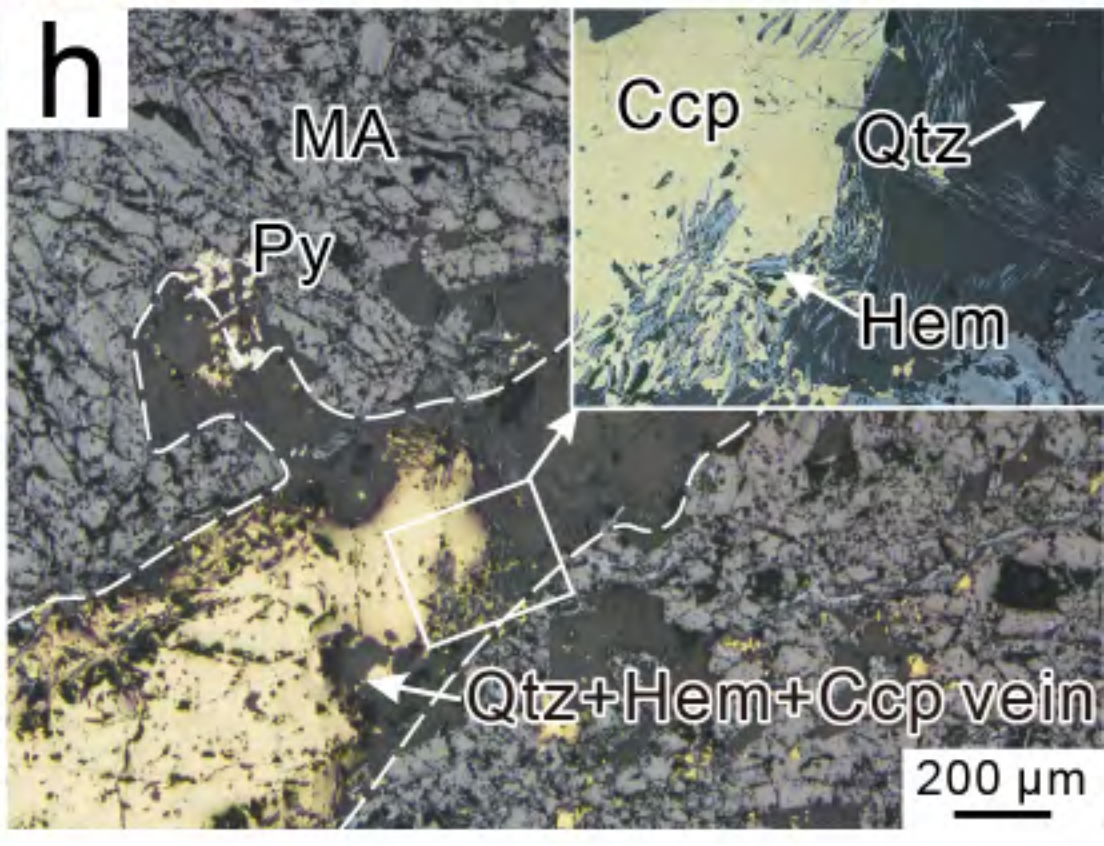
h
MA
Py
Ccp
Qtz
Hem
Qtz+Hem+Ccp vein
200 μm

Fig 4

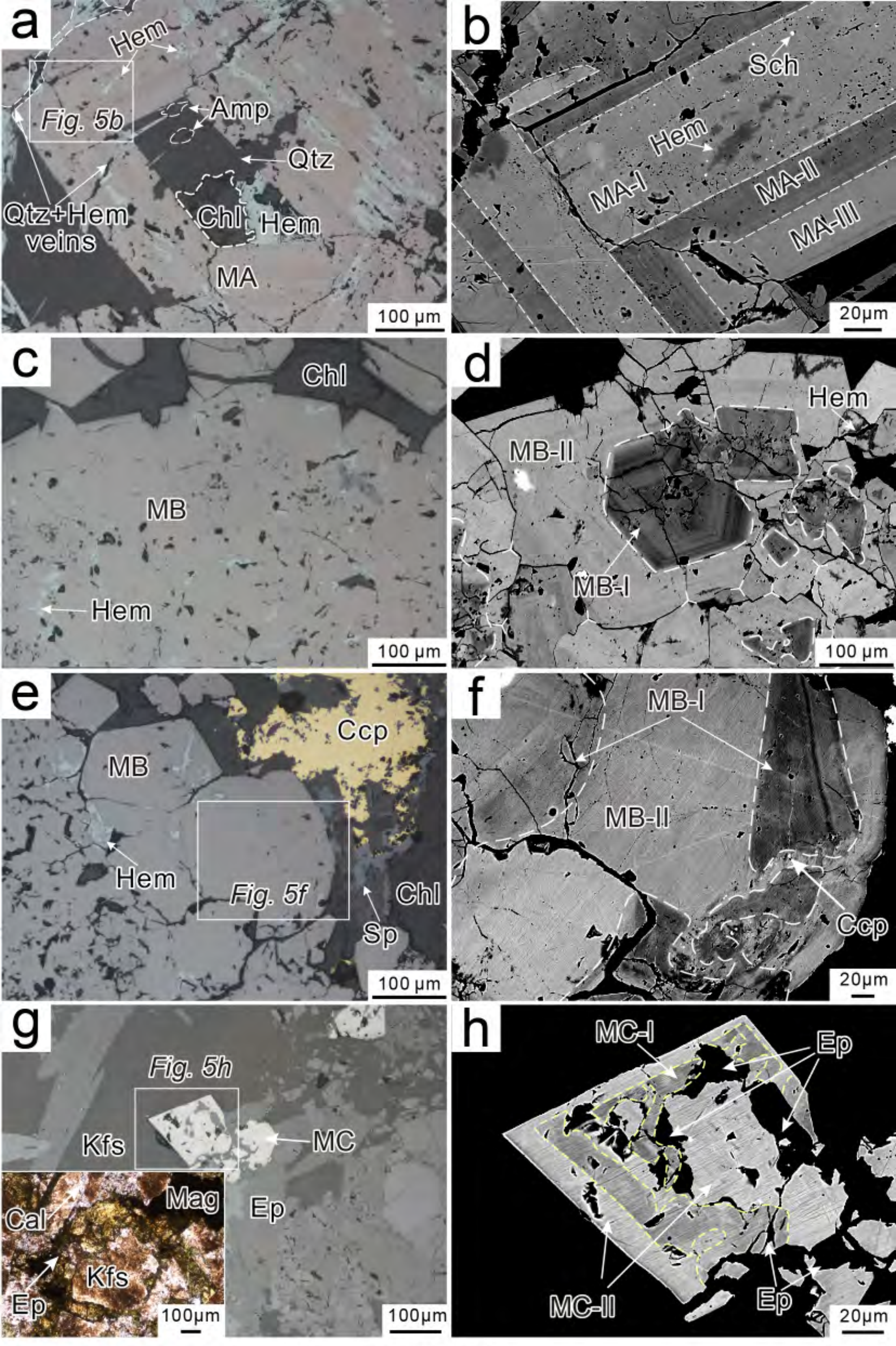
a
Hem
Fig. 5b
Amp
Qtz
Qtz+Hem veins
Chl
Hem
MA
100 μm
b
Sch
Hem
MA-I
MA-II
MA-III
20μm
c
Chl
MB
Hem
100 μm
d
Hem
MB-II
MB-I
100 μm
e
Ccp
MB
Hem
Fig. 5f
Chl
Sp
100 μm
f
MB-I
MB-II
Ccp
20μm
g
Fig. 5h
Kfs
MC
Cal
Mag
Kfs
Ep
100μm
Ep
100μm
h
MC-I
Ep
MC-II
Ep
20μm

Fig 5

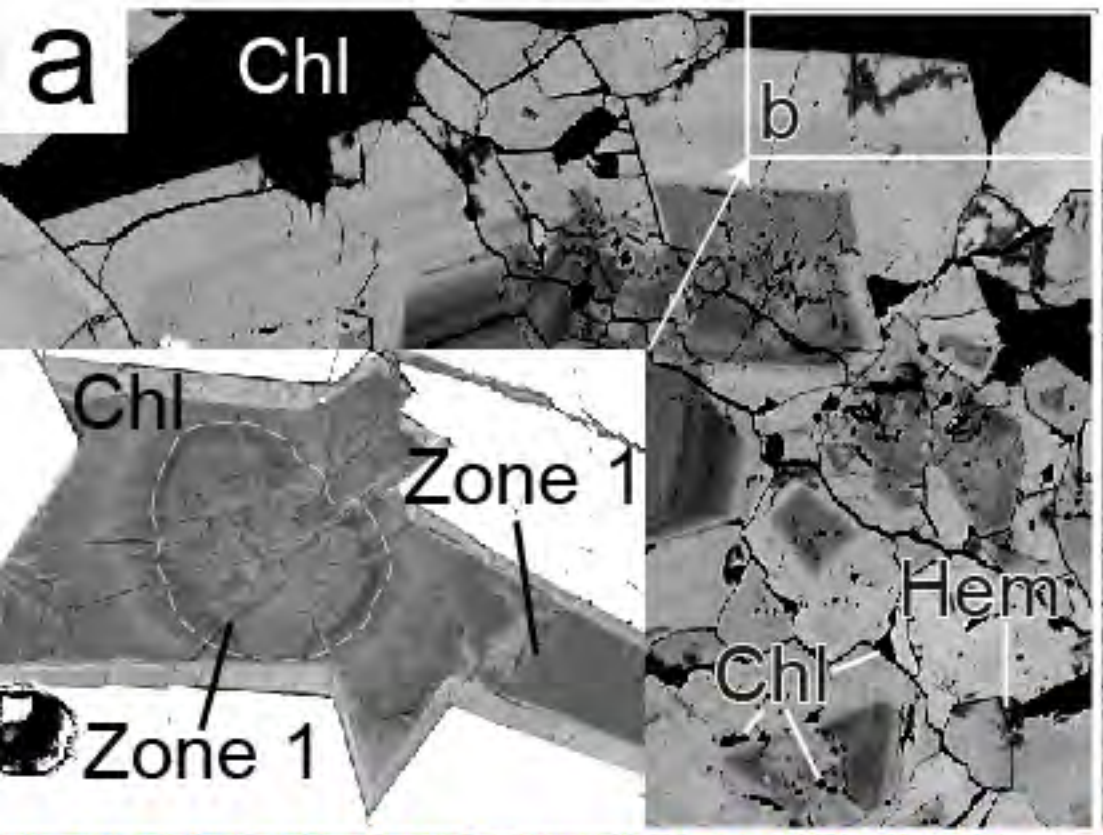
a
Chl
b
Chl
Zone 1
Zone 1
Hem
Chl

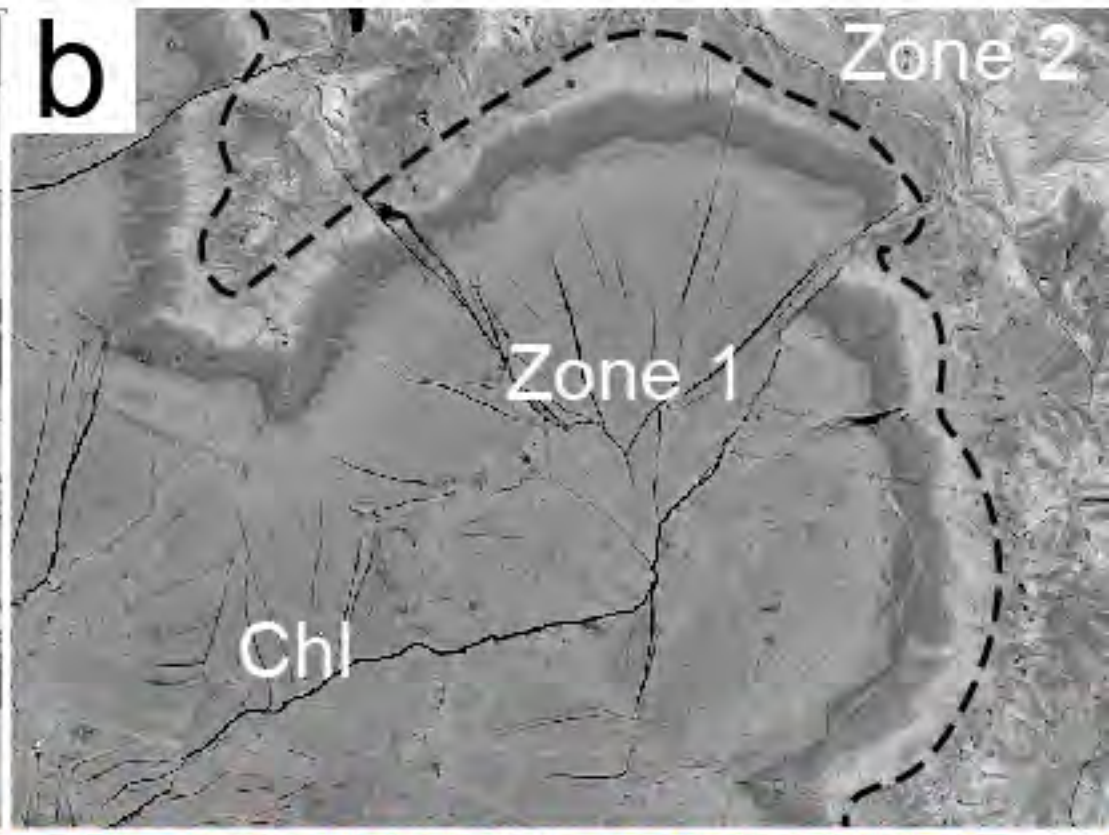
b
Zone 2
Zone 1
Chl

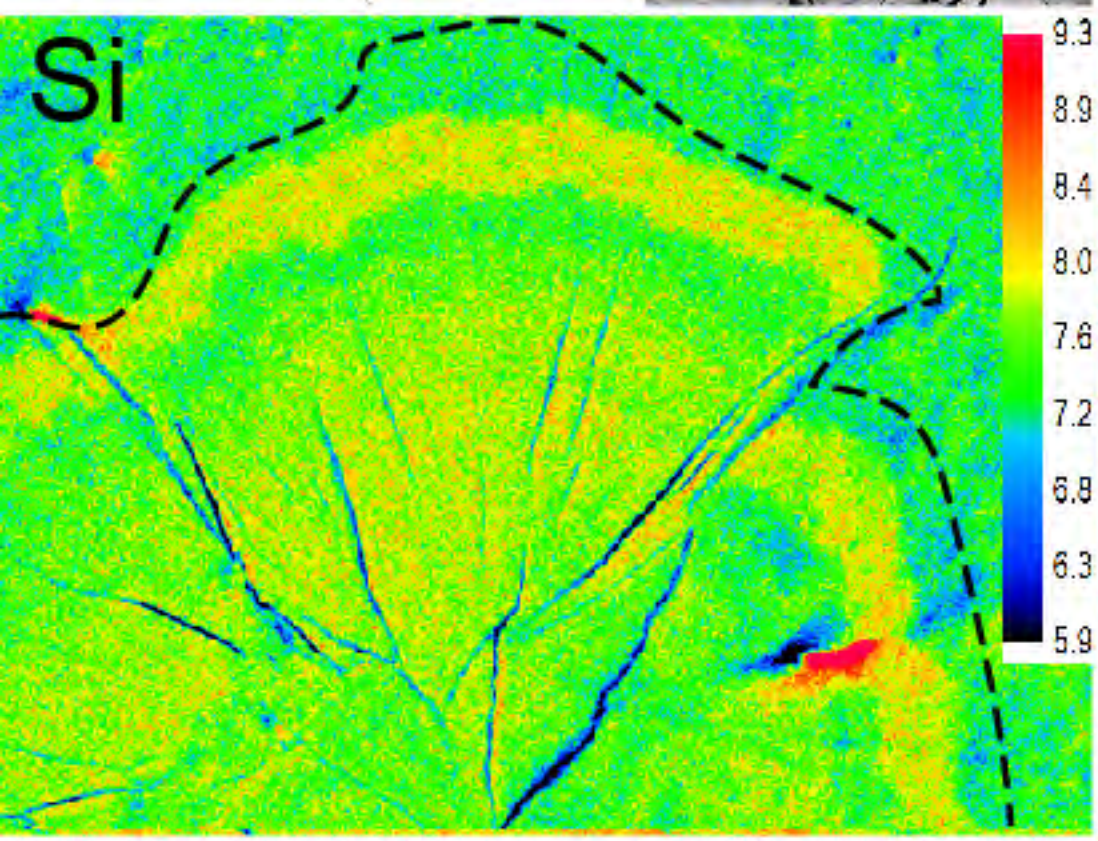
Si
9.3
8.9
8.4
8.0
7.6
7.2
6.8
6.3
5.9

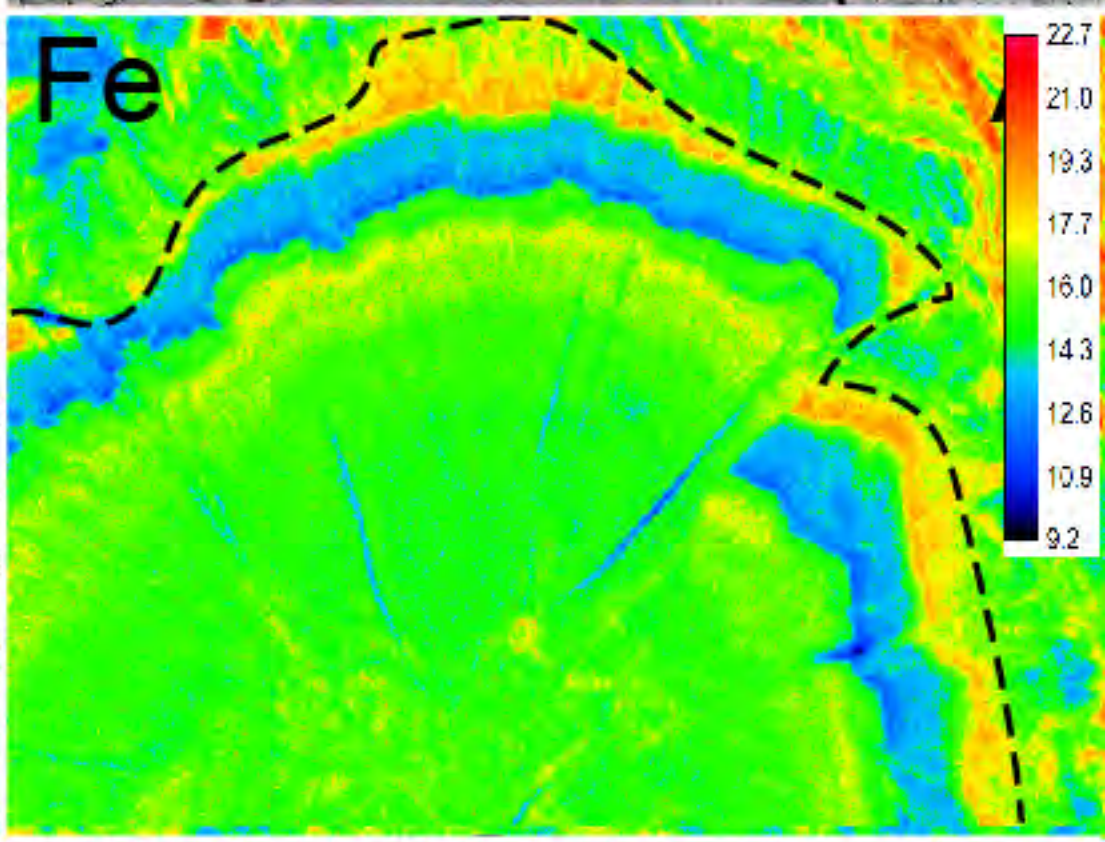
Fe
22.7
21.0
19.3
17.7
16.0
14.3
12.6
10.9
9.2

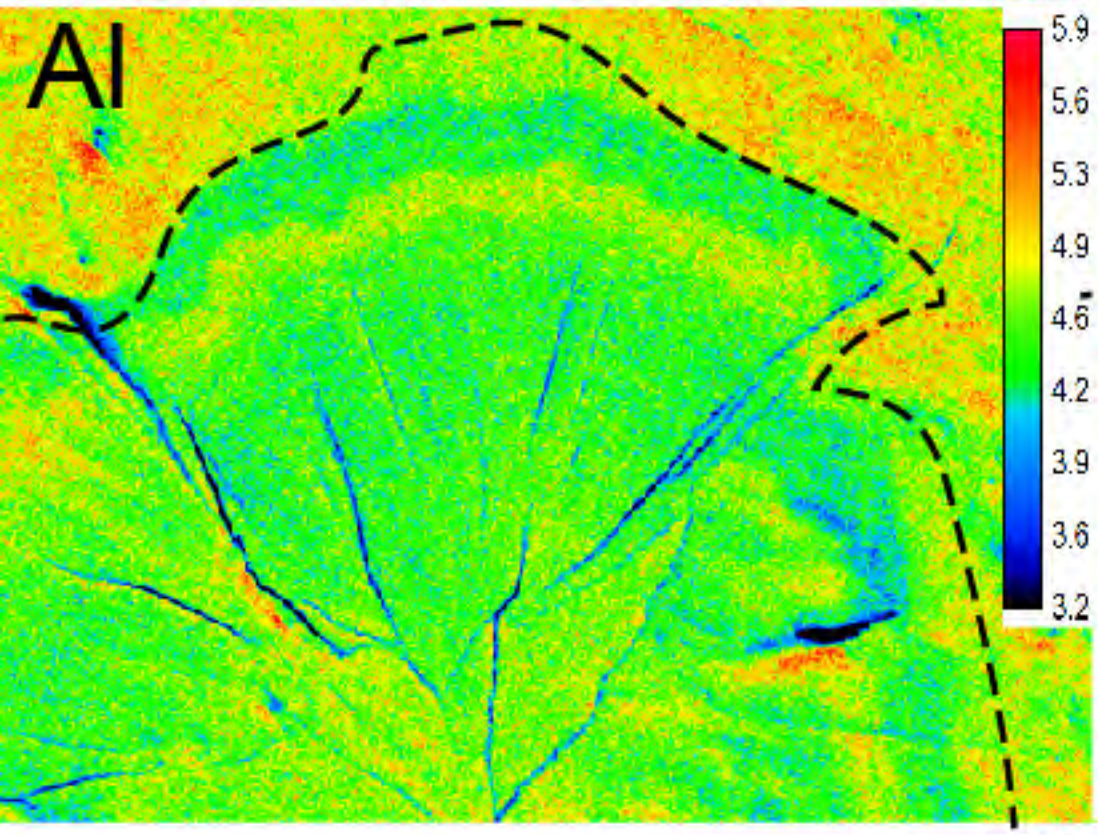
Al
5.9
5.6
5.3
4.9
4.6
4.2
3.9
3.6
3.2

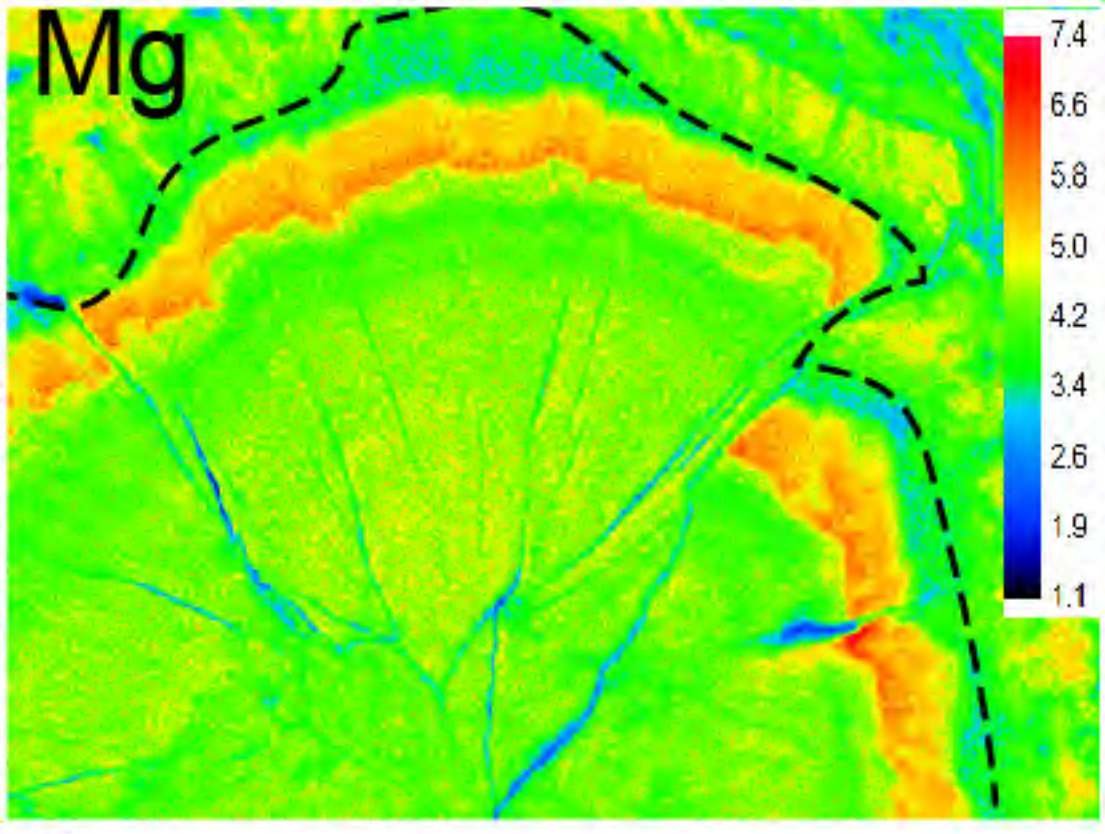
Mg
7.4
6.6
5.8
5.0
4.2
3.4
2.6
1.9
1.1

Fig 6

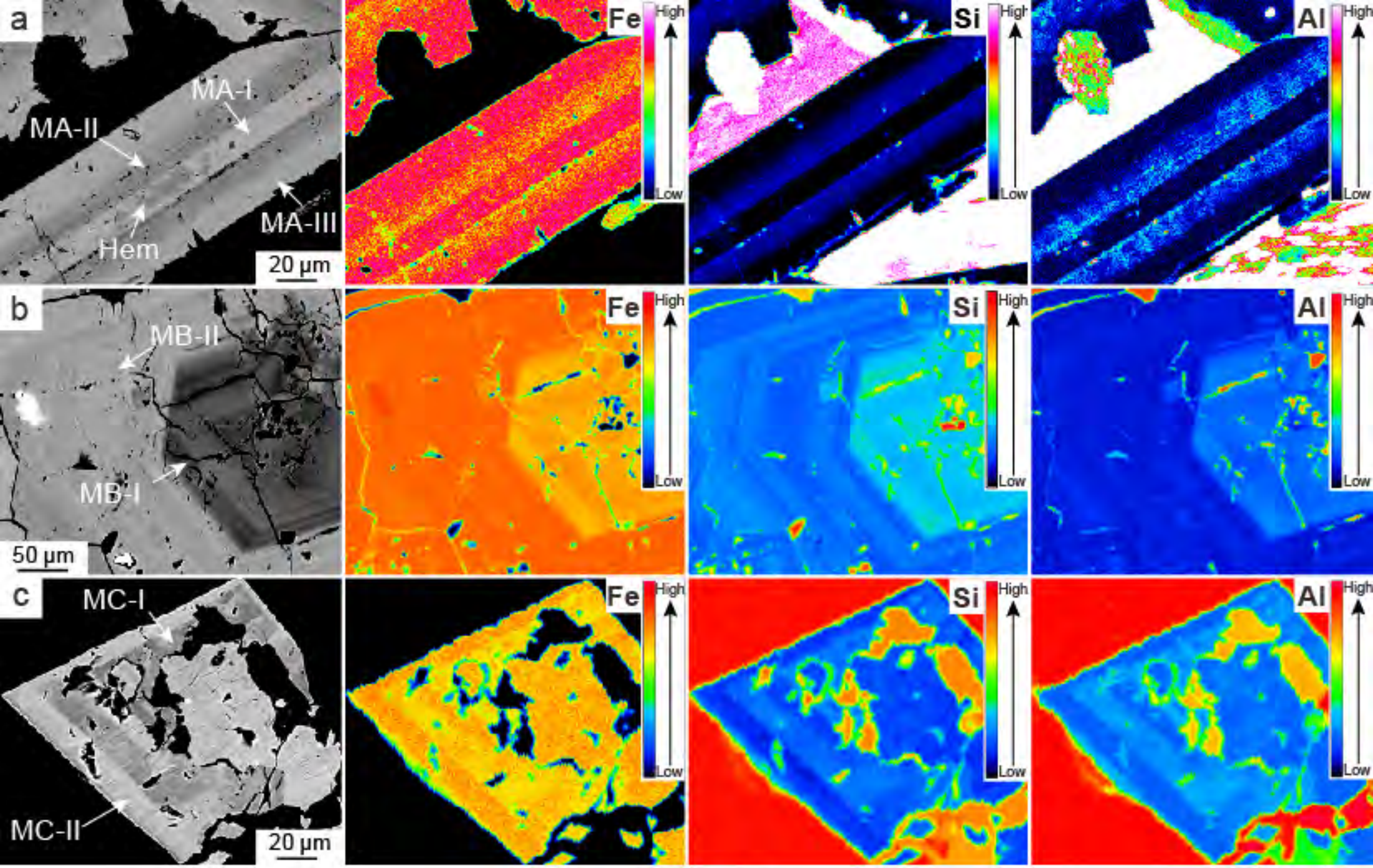
a
MA-I
MA-II
MA-III
Hem
20 μm
Fe
Si
Al
High
Low
b
MB-II
MB-I
50 μm
c
MC-I
MC-II
20 μm

Fig7

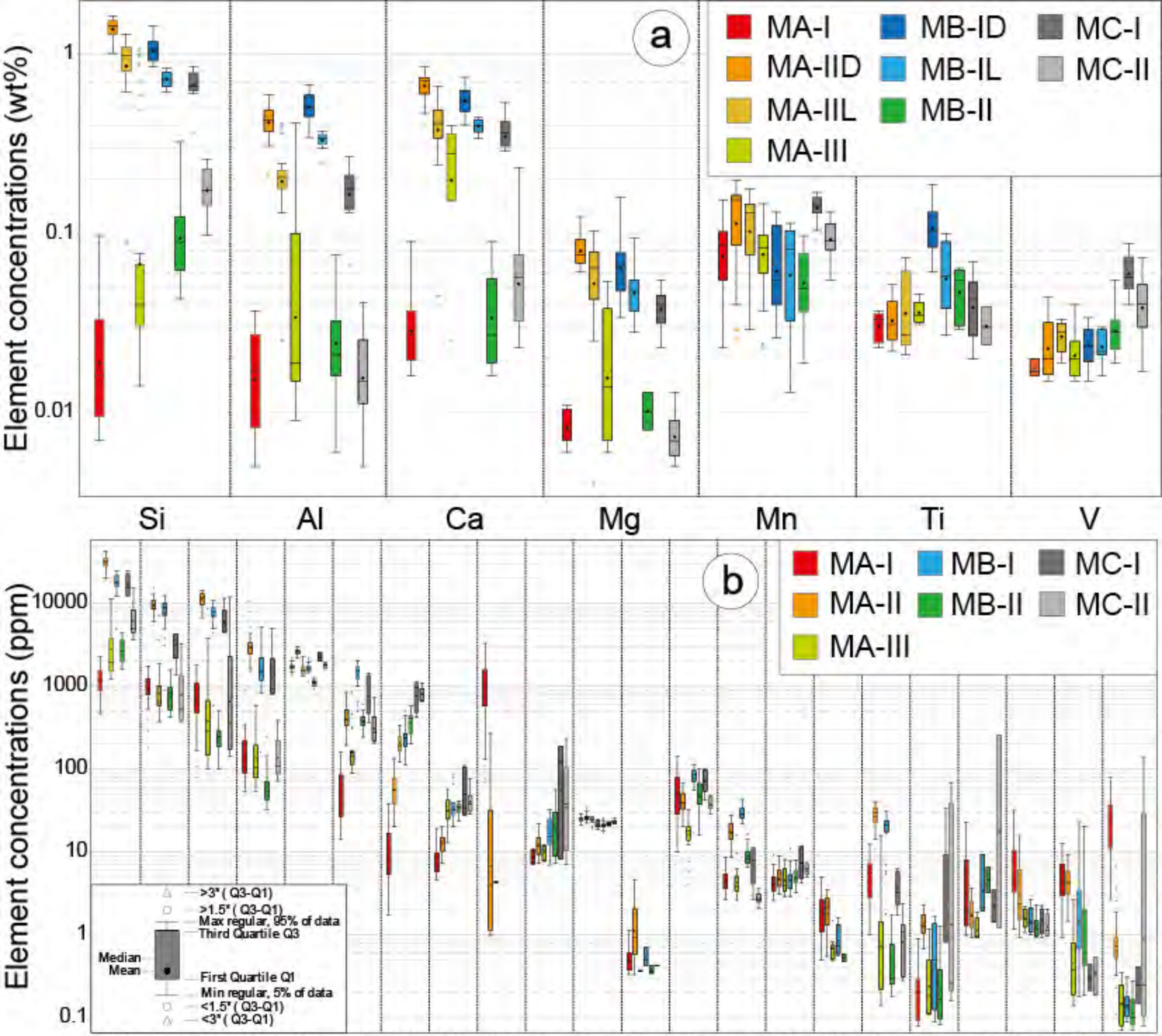
a
MA-I
MA-IID
MA-IIL
MA-III
MB-ID
MB-IL
MB-II
MC-I
MC-II
Element concentrations (wt%)
1
0.1
0.01
Si
Al
Ca
Mg
Mn
Ti
V
b
MA-I
MA-II
MA-III
MB-I
MB-II
MC-I
MC-II
Element concentrations (ppm)
10000
1000
100
10
1
0.1
>3* (Q3-Q1)
>1.5* (Q3-Q1)
Max regular, 95% of data
Third Quartile Q3
Median
Mean
First Quartile Q1
Min regular, 5% of data
<1.5* (Q3-Q1)
<3* (Q3-Q1)
Si Al Ca Mg Mn Ti V Ni W Cr Co Cu Zn Ga Ge Rb Sr Y Zr Sn Pb U

Fig 8

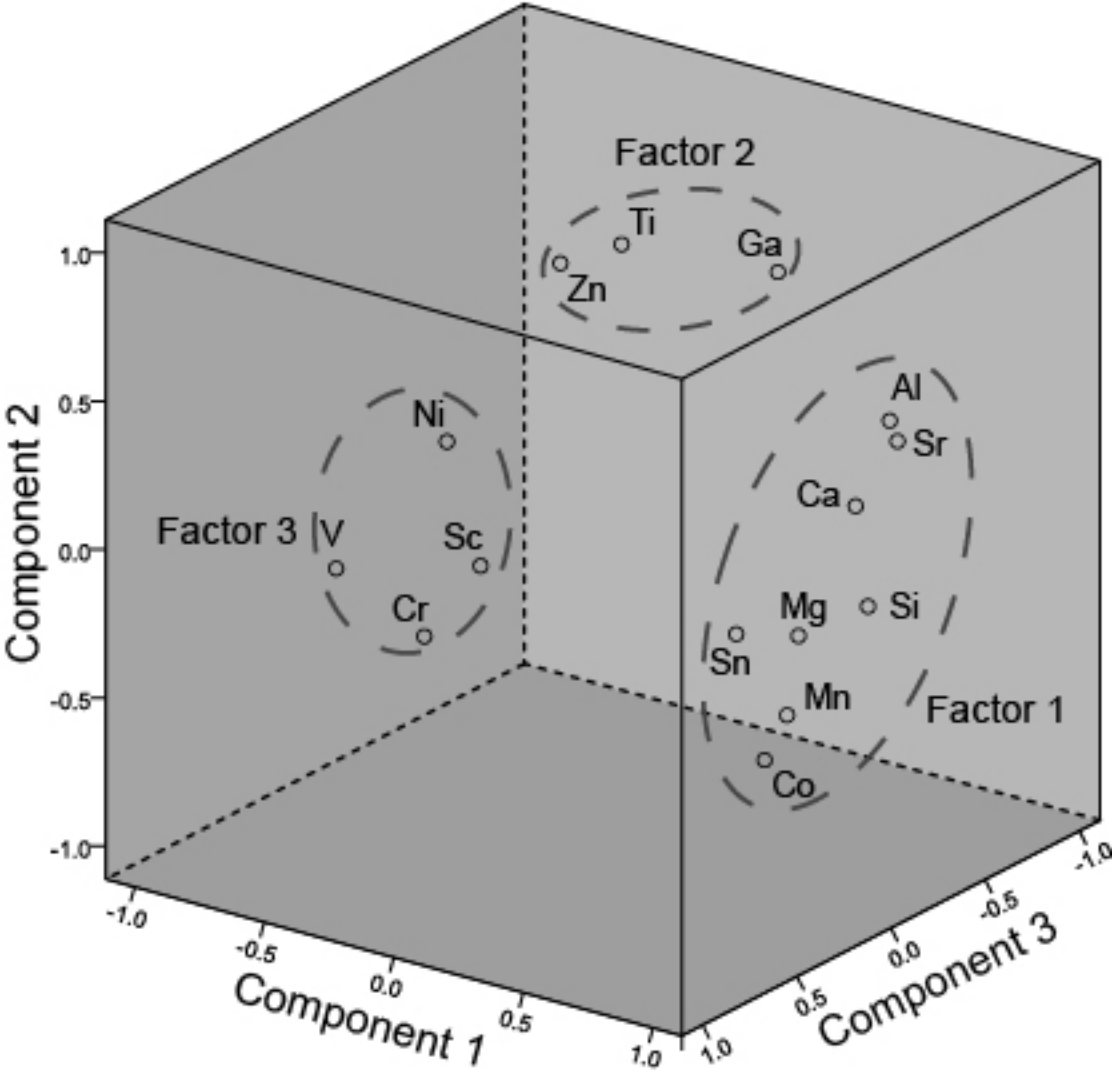
Factor 2
Ti
Ga
Zn
Ni
Factor 3
V
Sc
Cr
Al
Sr
Ca
Mg
Si
Sn
Mn
Co
Factor 1
Component 2
1.0
0.5
0.0
-0.5
-1.0
Component 1
-1.0
-0.5
0.0
0.5
1.0
Component 3
1.0
0.5
0.0
-0.5
-1.0

Fig 9

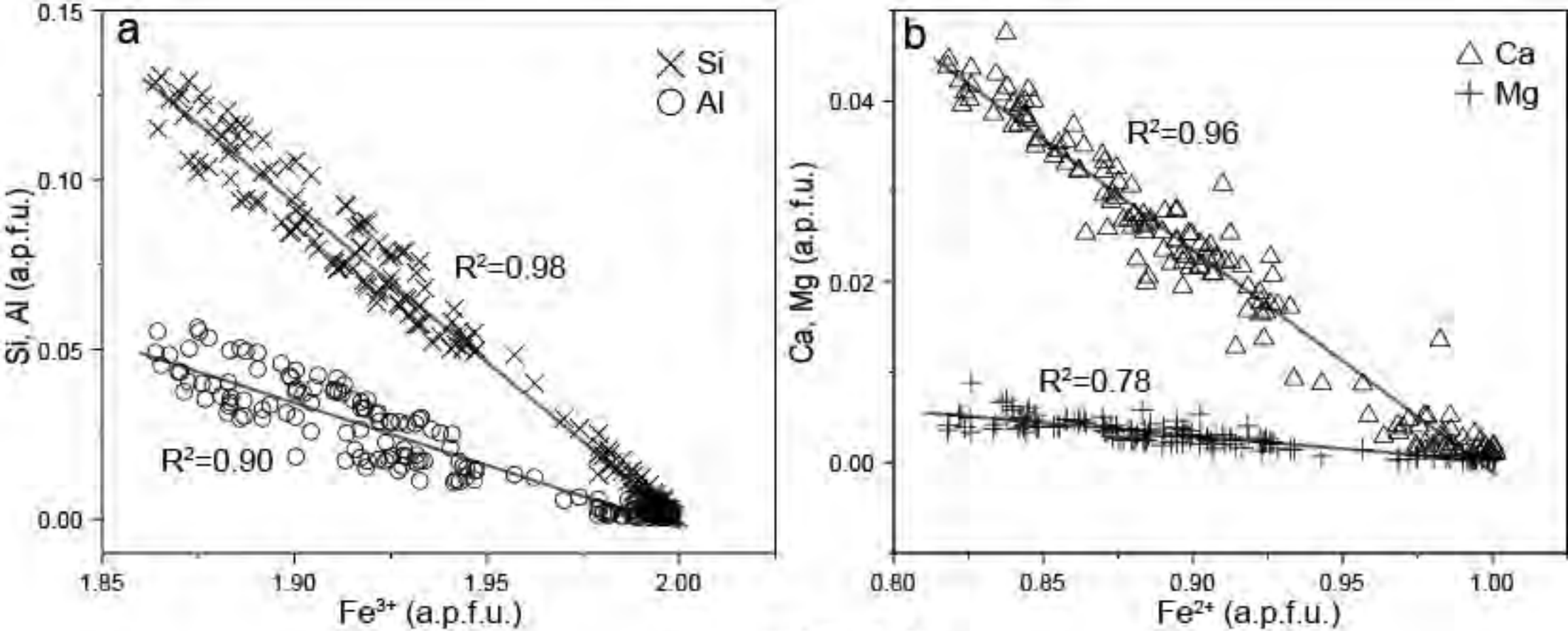
a
Si
Al
R²=0.98
R²=0.90
Si, Al (a.p.f.u.)
Fe³⁺ (a.p.f.u.)
0.15
0.10
0.05
0.00
1.85
1.90
1.95
2.00
b
Ca
Mg
R²=0.96
R²=0.78
Ca, Mg (a.p.f.u.)
Fe²⁺ (a.p.f.u.)
0.04
0.02
0.00
0.80
0.85
0.90
0.95
1.00

Fig 10

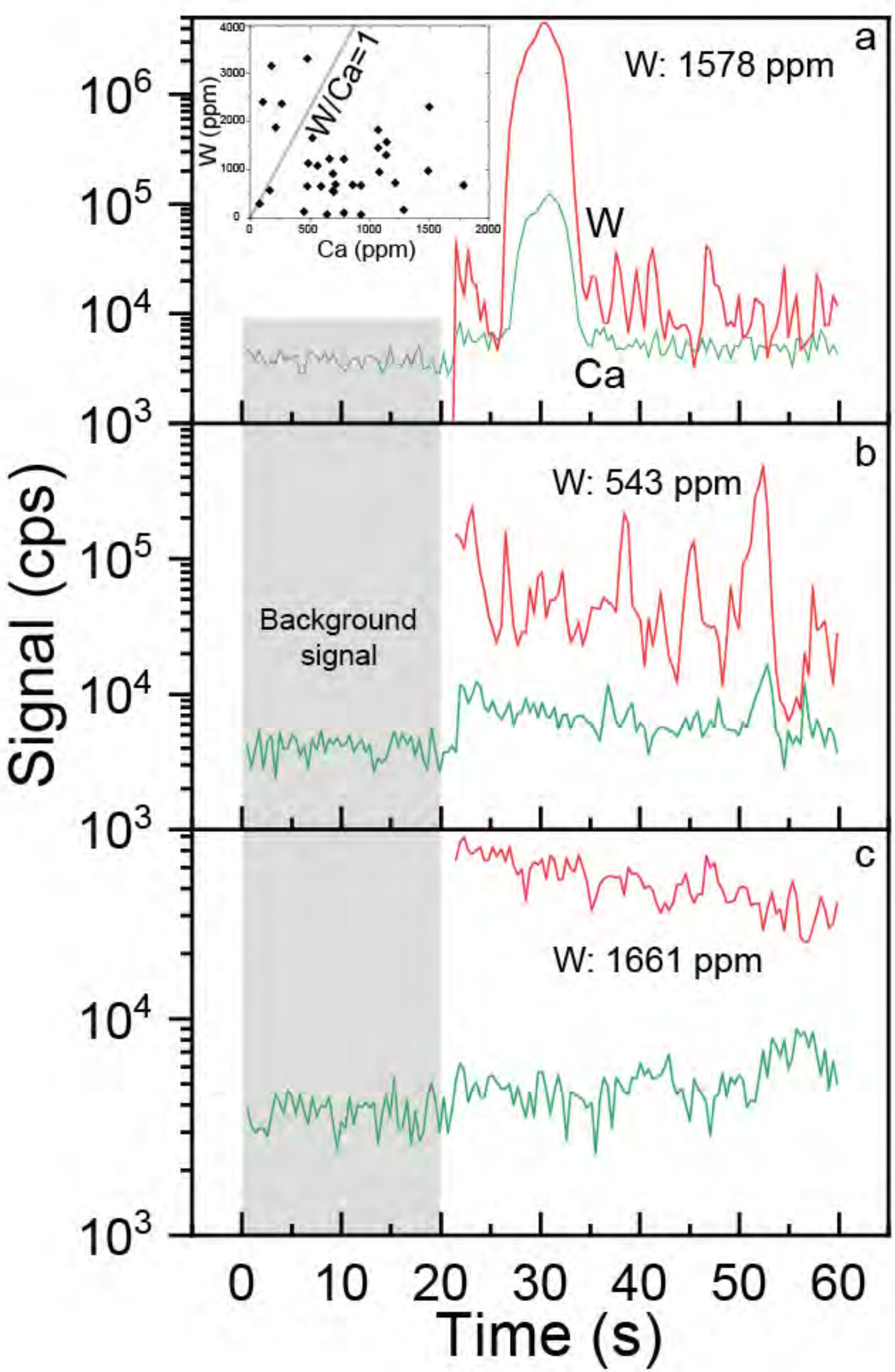
a
W: 1578 ppm
W
Ca
W (ppm)
Ca (ppm)
W/Ca=1
b
W: 543 ppm
Background signal
c
W: 1661 ppm
Signal (cps)
Time (s)

Fig 11

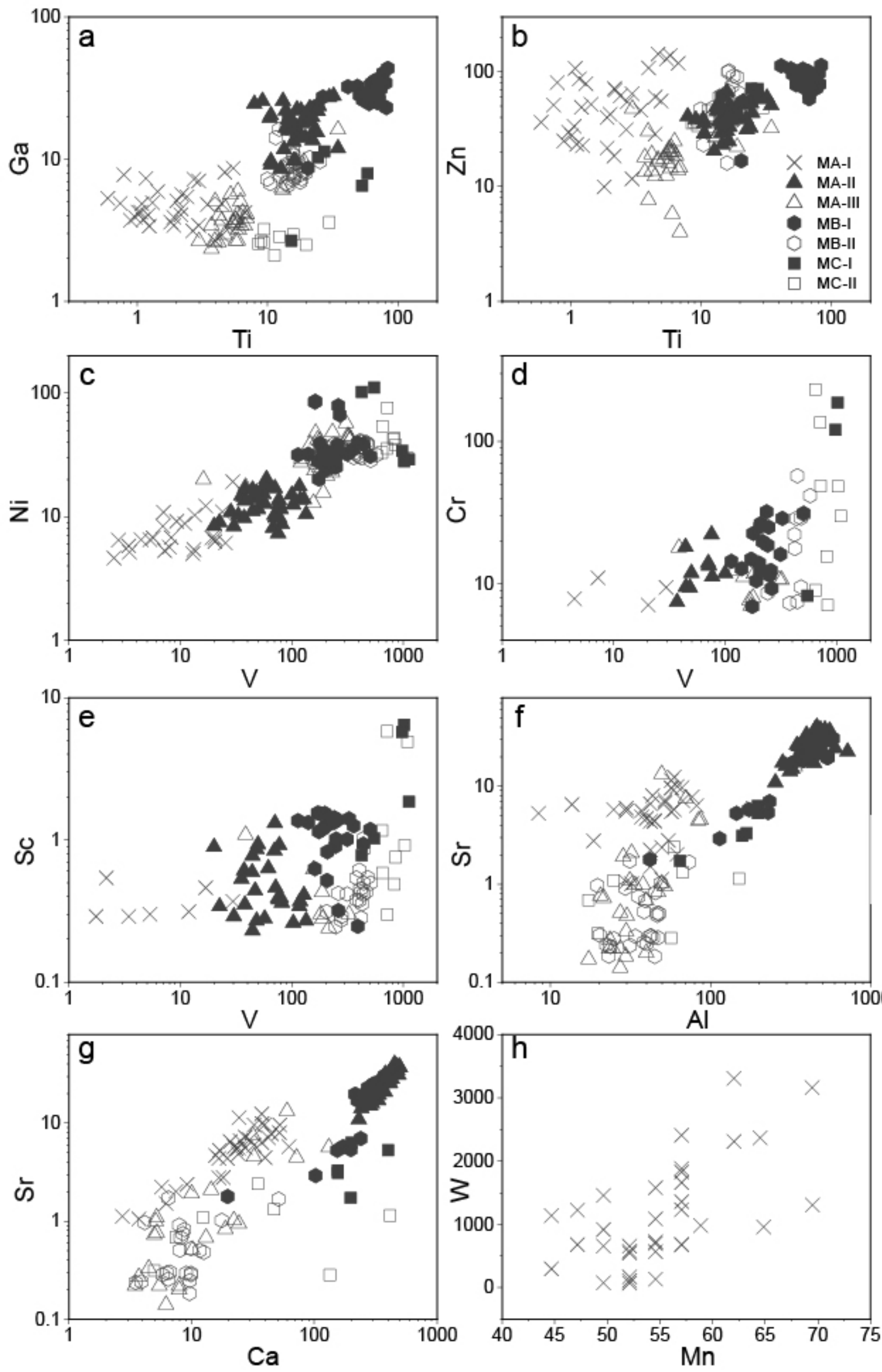
a
Ga
Ti
b
Zn
Ti
MA-I
MA-II
MA-III
MB-I
MB-II
MC-I
MC-II
c
Ni
V
d
Cr
V
e
Sc
V
f
Sr
Al
g
Sr
Ca
h
W
Mn

Fig 12

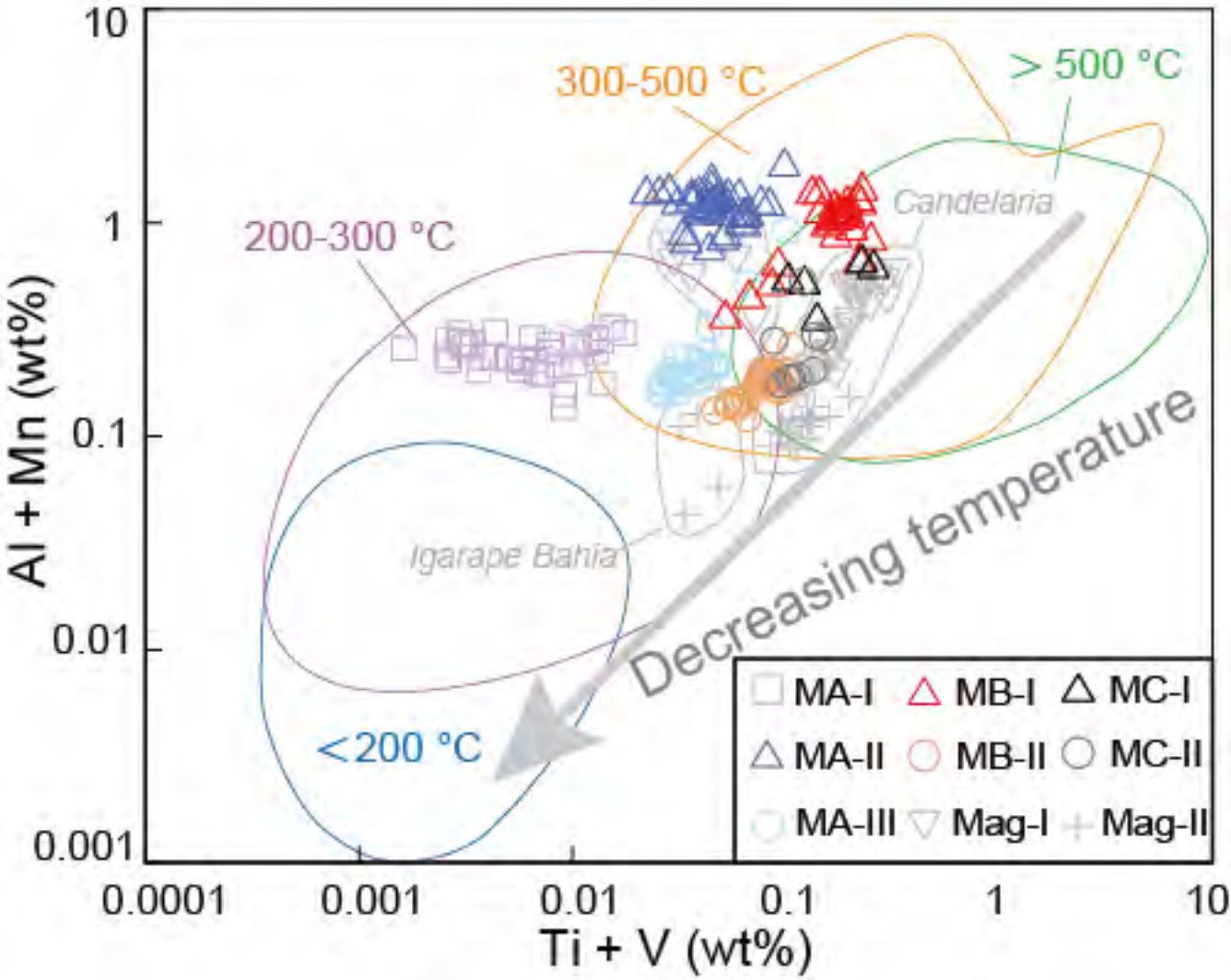
300-500 °C
> 500 °C
200-300 °C
Candelaria
Igarape Bahia
< 200 °C
Decreasing temperature
MA-I
MB-I
MC-I
MA-II
MB-II
MC-II
MA-III
Mag-I
Mag-II
Al + Mn (wt%)
Ti + V (wt%)
10
1
0.1
0.01
0.001
0.0001
0.001
0.01
0.1
1
10

Fig 13

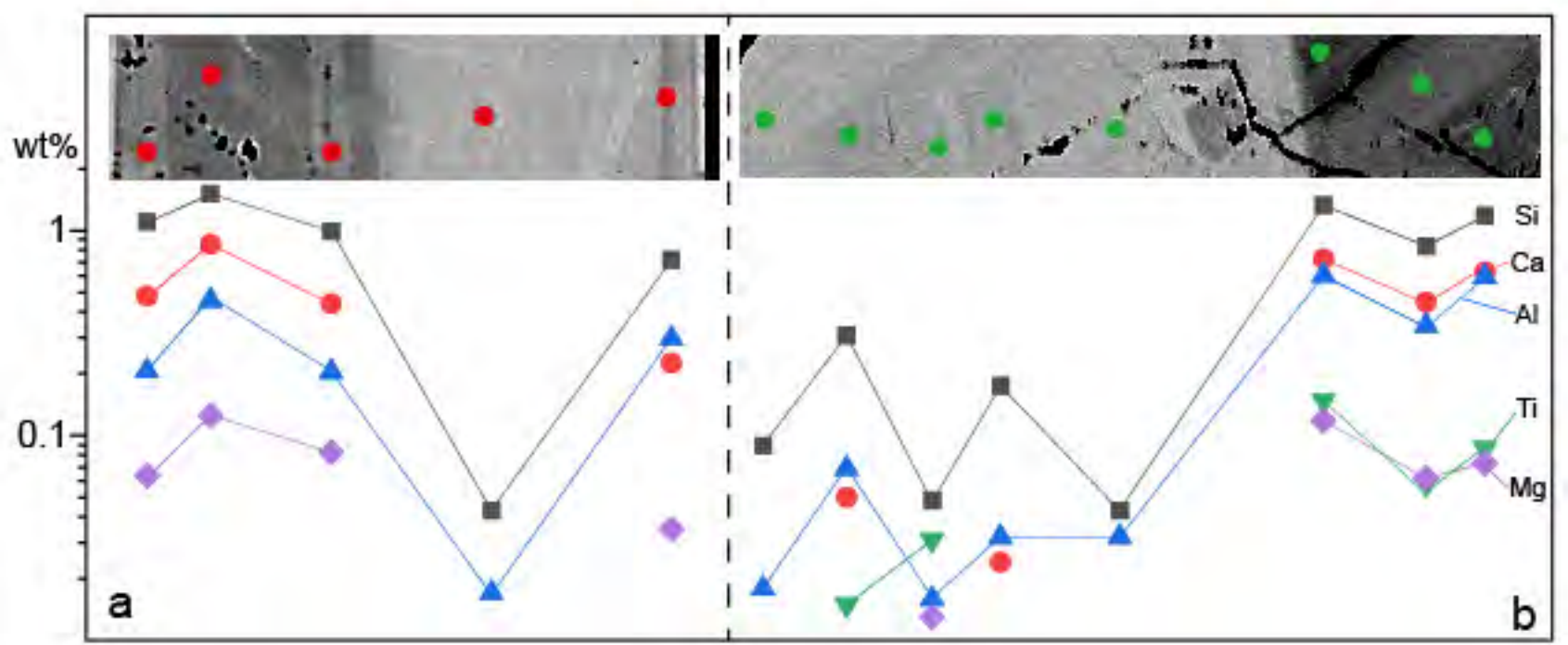

Fig 14